Neurobiology of Disease

Shared and Distinct Functional Effects of Patient-Specific *Tbr1* Mutations on Cortical Development

Marissa Co,[1,2] Rebecca A. Barnard,[1] Jennifer N. Jahncke,[2] Sally Grindstaff,[1] Lev M. Fedorov,[3] Andrew C. Adey,[1] Kevin M. Wright,[2] and Brian J. O'Roak[1]

[1]Department of Molecular and Medical Genetics, Oregon Health & Science University, Portland, Oregon 97239, [2]Vollum Institute, Oregon Health & Science University, Portland, Oregon 97239, and [3]Transgenic Mouse Models Core, Oregon Health & Science University, Portland, Oregon 97239

T-Box Brain Transcription Factor 1 (TBR1) plays essential roles in brain development, mediating neuronal migration, fate specification, and axon tract formation. While heterozygous loss-of-function and missense *TBR1* mutations are associated with neurodevelopmental conditions, the effects of these heterogeneous mutations on brain development have yet to be fully explored. We characterized multiple mouse lines carrying *Tbr1* mutations differing by type and exonic location, including the previously generated *Tbr1* exon 2-3 knock-out (KO) line, and we analyzed male and female mice at neonatal and adult stages. The frameshift patient mutation A136PfsX80 (A136fs) caused reduced TBR1 protein in cortex similar to *Tbr1* KO, while the missense patient mutation K228E caused significant TBR1 upregulation. Analysis of cortical layer formation found similar defects between KO and A136fs homozygotes in their CUX1$^+$ and CTIP2$^+$ layer positions, while K228E homozygosity produced layering defects distinct from these mutants. Meanwhile, the examination of cortical apoptosis found extensive cell death in KO homozygotes but limited cell death in A136fs or K228E homozygotes. Despite their discordant cortical phenotypes, these *Tbr1* mutations produced several congruent phenotypes, including anterior commissure reduction in heterozygotes, which was previously observed in humans with *TBR1* mutations. These results indicate that patient-specific *Tbr1* mutant mice will be valuable translational models for pinpointing shared and distinct etiologies among patients with *TBR1*-related developmental conditions.

Key words: autism; cortex; developmental biology; genetics; mouse; TBR1

Significance Statement

Mutations of the *TBR1* gene increase the likelihood of neurodevelopmental conditions such as intellectual disability and autism. Therefore, the study of *TBR1* can offer insights into the biological mechanisms underlying these conditions, which affect millions worldwide. To improve the modeling of *TBR1*-related conditions over current *Tbr1* knock-out mice, we created mouse lines carrying *Tbr1* mutations identical to those found in human patients. Mice with one mutant *Tbr1* copy show reduced amygdalar connections regardless of mutation type, suggesting a core biomarker for *TBR1*-related disorders. In mice with two mutant *Tbr1* copies, brain phenotypes diverge by mutation type, suggesting differences in *Tbr1* gene functionality in different patients. These mouse models will serve as valuable tools for understanding genotype–phenotype relationships among patients with neurodevelopmental conditions.

Introduction

Neurodevelopmental conditions such as developmental delay (DD), intellectual disability (ID), and autism impact numerous individuals and their caretakers worldwide (American Psychiatric Association, 2013). These conditions are highly heritable, yet their genetic architectures encompass a vast allelic spectrum and pleiotropic effects of multiple loci (Iakoucheva et al., 2019; Lee et al., 2019). A large contributor to the likelihood of these conditions is *de novo* mutations, accounting for 30–50% of cases (Hamdan et al., 2014; Iossifov et al., 2014; McRae et al., 2017; Yoon et al., 2021). Such mutations are informative for understanding their biological mechanisms, as they typically induce large phenotypic effect sizes and impact single genes.

Received Feb. 28, 2022; revised July 6, 2022; accepted July 30, 2022.

Author contributions: M.C., R.A.B., L.M.F., A.C.A., K.M.W., and B.J.O. designed research; M.C., R.A.B., J.N.J., S.G., and L.M.F. performed research; M.C., J.N.J., and S.G. analyzed data; M.C. wrote the paper.

This work was supported by National Institutes of Health Grant R01-MH-113926 (to B.J.O.) and an Oregon Health & Science University (OHSU) Shared Resources Pilot Award (to B.J.O.). We thank current and former members of the O'Roak, Wright, and Adey laboratory groups for feedback and technical support, including Dominica Cao, Brooke DeRosa, Sara Evans-Dutson, Bridget Fitzgerald, Destine Krenik, Cierra LeBlanc, Neville Lee, Amanda Mar, Ryan Mulqueen, Andrew Nishida, and Lindsay Wourms. We also thank Yingming Wang at the OHSU Transgenic Mouse Models Core for assistance with generating mouse lines. In addition, we thank the following current and past members of the BRAINS R01 Advisory Committee: Eric Fombonne, Marc Freeman, Gail Mandel, Tomasz Nowakowski, and Soo-Kyung Lee.

The authors declare no competing financial interests.

Correspondence should be addressed to Brian J. O'Roak at oroak@ohsu.edu.

https://doi.org/10.1523/JNEUROSCI.0409-22.2022

TBR1 (T-Box Brain Transcription factor 1) was among the first genes linked to ID and/or autism via *de novo* mutations (Neale et al., 2012; O'Roak et al., 2012a,b, 2014). Over 100 variants impacting *TBR1* have been reported in ClinVar, and *TBR1* is highly intolerant to both loss-of-function and missense mutations (Landrum et al., 2018; Karczewski et al., 2020). Accordingly, no biallelic *TBR1* mutations have been identified in humans, and $Tbr1^{-/-}$ mice die perinatally (Bulfone et al., 1998; Nambot et al., 2020). The spatiotemporal expression of *TBR1* in human brain places it at the center of an autism-associated gene network specific to mid-fetal glutamatergic cortical neurons (Willsey et al., 2013). During the equivalent period in mouse cortex, TBR1 directly regulates the transcription of other high-confidence autism-associated genes (Notwell et al., 2016). *Tbr1* is expressed in several early-born neuronal populations essential for proper mouse corticogenesis, and complete genetic knock-out (KO) consequently impairs cortical lamination, cell survival, neuronal fate acquisition, and axon tract formation (Hevner et al., 2001; Bedogni et al., 2010; Han et al., 2011; McKenna et al., 2011).

Individuals with *de novo TBR1* mutations exhibit moderate-to-severe DD/ID, speech delays, autism or autistic traits, and aggression (McDermott et al., 2018; Nambot et al., 2020). Over half of patients examined by MRI showed anterior commissure (AC) reduction, hippocampal dysplasia, and/or cortical malformations (Vegas et al., 2018; Nambot et al., 2020). Likewise, heterozygous *Tbr1* knock-out mice ($Tbr1^{+/-}$) modeling human *TBR1* haploinsufficiency showed anterior commissure reduction, cognitive impairment, and reduced social interaction (Huang et al., 2014). Mouse models in which *Tbr1* was conditionally deleted ($Tbr1^{cKO}$) from cortical deep-layer glutamatergic neurons also showed reduced social interaction or increased aggression (Fazel Darbandi et al., 2018, 2020). While both $Tbr1^{+/-}$ and $Tbr1^{cKO}$ models showed congruent defects in dendritic spine density, $Tbr1^{cKO}$ models may have limited clinical translatability because of the delayed deletion of *Tbr1* several days after its initial expression. Moreover, *Tbr1* deletion models do not capture the allelic heterogeneity of human *TBR1* mutations, and *in vitro* studies indicate that mutant TBR1 proteins differ in their stability, transcriptional activity, localization, and cofactor binding (Deriziotis et al., 2014; den Hoed et al., 2018).

Mice harboring the K228E patient mutation in the T-box of TBR1 were recently generated and characterized (Yook et al., 2019). In contrast to *Tbr1* deletion mutants, K228E mutants showed elevated levels of TBR1 protein, and the mutant K228E protein exhibited decreased DNA affinity and increased structural stability *in vitro*. Moreover, K228E mutants showed altered anxiety-like and social behaviors, which were accompanied by transcriptional dysregulation, displacement of parvalbumin (PV)-positive interneurons, and increased inhibitory synaptic transmission in the cortex. However, the degree of functionality of the mutant allele remains unclear, as do its effects on other *Tbr1*-regulated processes such as axon tract formation and cell survival.

Here, we independently generated *Tbr1* mutant mice with the K228E mutation, as well as mice with the early-truncating frameshift patient mutation A136PfsX80 (A136fs). We also characterized an in-frame *Tbr1* deletion line (p.E348_P353del or Δ6aa) encompassing five reported human *TBR1* variants in the T-box. With the *Tbr1* exon 2-3 knockout as a comparison (Bulfone et al., 1998), we used molecular, histologic, and genetic approaches to determine the impacts of these mutations on *Tbr1* expression and cortical development.

Materials and Methods

Experimental design and statistical analysis. Mice of each sex were used for all experiments. For molecular and histologic experiments, mice were analyzed at postnatal day 0 (P0) or adulthood (9–39 weeks). For weight and behavior assessments, mice were analyzed at P4, P7, P10, and P14. Cohorts for each experiment were composed of littermate wild-type (WT) and mutant mice from at least two independent litters. For Western blot and quantitative PCR (qPCR) experiments, at least three mice/genotype/line were analyzed. For histologic experiments, at least two mice/genotype/line were analyzed. Data plotting and statistical tests were performed using Prism 9 (GraphPad Software). Data are represented as the mean ± SEM or as violin plots. Each dot represents one animal where applicable. Analyses between two groups were performed using unpaired *t* tests. Analyses among three groups were performed using one-way ANOVA with Tukey's multiple-comparisons test or two-way ANOVA with Šidák's multiple-comparisons test. Analysis of postnatal weight and motor assessment was performed using two-way repeated-measures ANOVA with Šidák's multiple-comparisons test. Analysis of cumulative interneuron distribution was performed using Kolmogorov–Smirnov tests. Significance was defined as $p < 0.05$.

Animals. All animal procedures were approved by Oregon Health & Science University Institutional Animal Care and Use Committee. $Tbr1^{KO}$ mice (Bulfone et al., 1998) were rederived from cryopreserved sperm obtained from MMRRC (Mutant Mouse Resource & Research Centers) at the University of California, Davis (catalog #030263-UCD) and backcrossed to a C57BL/6 background for at least two generations before data collection. $Tbr1^{A136PfsX80}$ (abbreviated to $Tbr1^{A136fs}$), $Tbr1^{K228E}$, and $Tbr1^{\Delta 6aa}$ mice were generated on a C57BL/6NJ background and backcrossed to C57BL/6NJ for at least two generations before data collection. $Tbr1^{KO}$ mice were PCR genotyped using primers amplifying genomic *Tbr1* and the neomycin (neo) cassette. $Tbr1^{A136fs}$ and $Tbr1^{K228E}$ mice were genotyped using PCR amplification of the mutation-containing genomic region followed by restriction enzyme digest of the PCR product (BtsCI for A136fs, BtsIMutI for K228E, New England Biolabs). $Tbr1^{\Delta 6aa}$ mice were PCR genotyped using primers amplifying genomic *Tbr1* (Extended Data Fig. 1-2, primer sequences). Mice were group housed under a 12 h light/dark cycle and given *ad libitum* access to food and water.

CRISPR generation of mouse lines. CRISPR synthetic guide RNA (sgRNA) design to generate $Tbr1^{A136fs}$, $Tbr1^{K228E}$, and $Tbr1^{\Delta 6aa}$ founders was performed using the CRISPOR tool (http://crispor.tefor.net/; Concordet and Haeussler, 2018). The generation of mutant mice was performed by the Oregon Health & Science University Transgenic Mouse Models Core based on published methods (Aida et al., 2015). C57BL/6NJ zygotes were coinjected with Cas9 protein (50 ng/μl; New England Biolabs) or *Cas9* mRNA (1000 ng/μl; TriLink BioTechnologies), sgRNA (30 ng/μl; Synthego), and single-stranded-oligodeoxynucleotide (ssODN) donor (100 ng/μl; Integrated DNA Technologies) containing the patient mutation. Embryos were transplanted into pseudopregnant recipient female CD-1 mice, and founders from these litters were identified via Sanger sequencing (Extended Data Fig. 1-2, sgRNA, ssODN donor, and Sanger primer sequences).

Western blotting. Cortex was dissected at P0 or adulthood (10–39 weeks), flash frozen, and stored at −80°C until all samples were collected. Frozen tissue from one cortical hemisphere per mouse (~30 mg at P0, ~100 mg at adulthood) was dounce homogenized in ice-cold RIPA buffer (150 mM NaCl, 1% IGEPAL CA-630, 0.5% sodium deoxycholate, 0.1% SDS, 50 mM Tris-HCl pH 8.0, 2 mM EDTA pH 8.0) containing Protease Inhibitor Cocktail (Roche). Nuclei were lysed using a probe sonicator (model XL-2000, Misonix) at setting 6 with 5–10 s ON/20 s OFF intervals until the lysate was clear (two rounds for P0, four to five rounds for adult). Lysates were further incubated on ice for 30 min then centrifuged at 10,000 relative centrifugal force for 10 min at 4°C to remove debris. Protein concentrations were determined using the Pierce BCA Protein Assay Kit (Thermo Fisher Scientific). Alfa Aesar Laemmli SDS sample buffer (Thermo Fisher Scientific) was added to lysates, which were boiled at 95°C for 5 min before SDS-PAGE. Total protein (30 μg/sample) was resolved on 4–15% polyacrylamide gels (BIO-RAD) and transferred to PVDF membranes. Membranes were incubated in

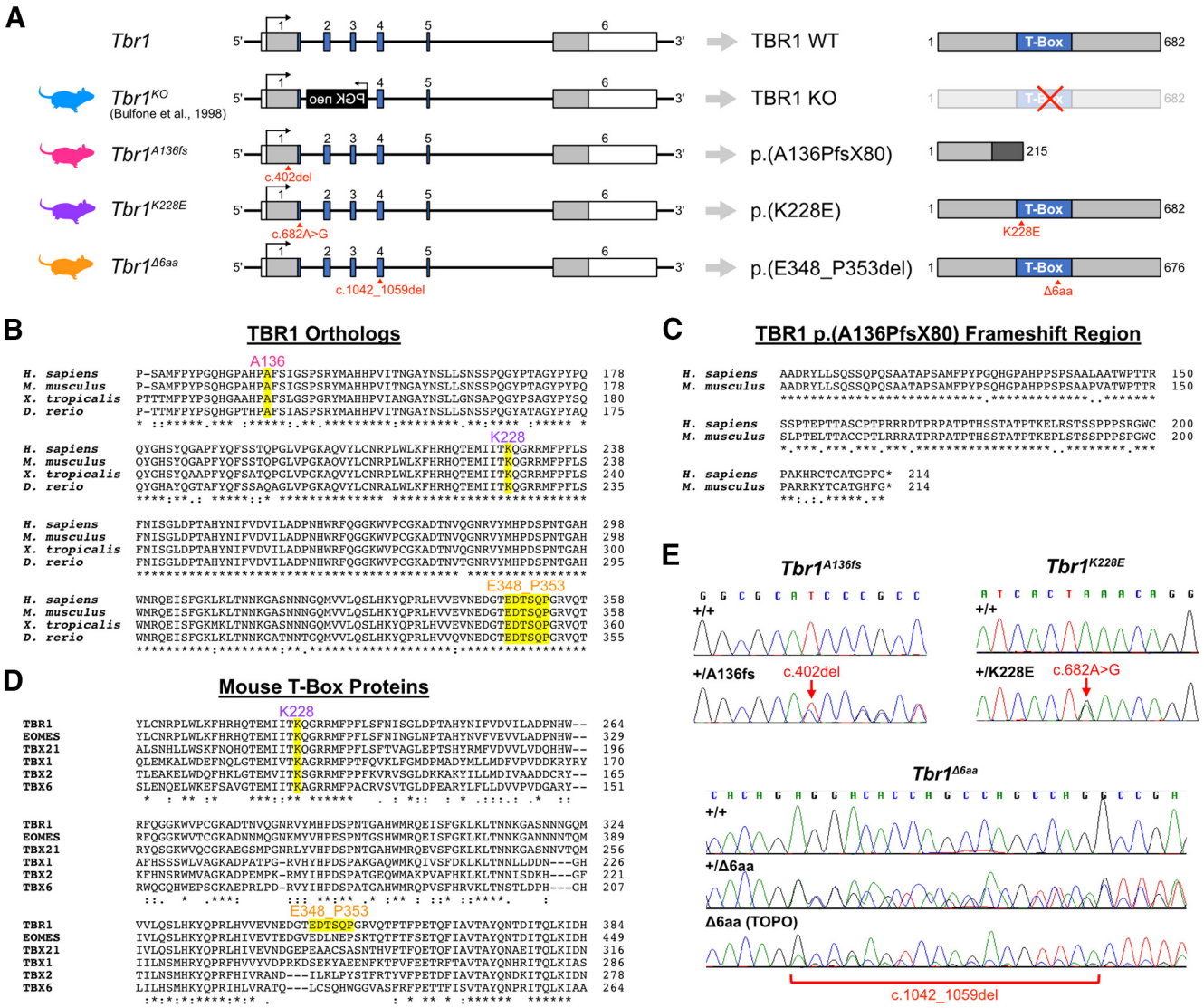

Figure 1. Generation of mouse lines carrying *Tbr1* mutations. ***A***, Schematic of *Tbr1* gene structure (left) and predicted protein products (right) for *Tbr1* mutant mouse lines used in this study: published $Tbr1^{KO}$ line replacing exons 2-3 with a neomycin cassette (Bulfone et al., 1998) and three CRISPR-generated lines carrying a frameshift mutation (A136PfsX80 or A136fs), missense mutation (K228E), or in-frame deletion of 6 aa (E348_P353del or Δ6aa). See Extended Data Figure 1-1 for reported human mutations within the in-frame deletion site of $Tbr1^{\Delta 6aa}$ mice. For *Tbr1* gene, blue boxes indicate T-box coding sequence, gray boxes indicate other coding sequence, and white boxes indicate untranslated regions. ***B***, Multiple sequence alignment of TBR1 mutation sites across vertebrate species. ***C***, Pairwise alignment of predicted frameshift regions of human and mouse TBR1-A136PfsX80 proteins. ***D***, Multiple sequence alignment of K228 and E348_P353 sites across mouse T-box family proteins. ***E***, Sanger sequencing of genomic or TOPO-cloned DNA showing CRISPR-generated $Tbr1^{A136fs}$, $Tbr1^{K228E}$, and $Tbr1^{\Delta 6aa}$ mutations. See Extended Data Figure 1-2 for CRISPR oligonucleotide and Sanger primer sequences. ***F***, Dorsal view of brains from postnatal day 0 $Tbr1^{A136fs}$, $Tbr1^{K228E}$, and $Tbr1^{\Delta 6aa}$ mutant mice and wild-type littermates. Arrowheads indicate underdeveloped olfactory bulbs in $Tbr1^{A136fs/A136fs}$ and $Tbr1^{K228E/K228E}$ mice. Scale bar, 1 mm.

block solution [5% milk in TBS with 0.1% Tween-20 (TBST)] for 1 h at room temperature (RT), incubated in primary antibodies in block solution overnight at 4°C, washed in TBST four times for 5 min each, incubated in secondary antibodies in block solution for 1 h at room temperature, washed in TBST four times for 5 min each, and imaged with an Odyssey CLx using Image Studio software (LI-COR). The following primary antibodies and dilutions were used: rabbit anti-TBR1 (1:1000; catalog #ab31940, Abcam); rabbit anti-β-Tubulin III (1:1000; catalog #T2200, Sigma-Aldrich). The following secondary antibody and dilution was used: donkey anti-rabbit IgG IRDye 800CW (1:10,000; catalog #926–32213, LI-COR). Western blot band intensities were measured using "Analyze > Gels" in ImageJ2/FIJI software (Rueden et al., 2017). Within each blot, each TBR1 band signal was normalized to its corresponding loading control signal, and then each normalized TBR1 signal was adjusted to the average normalized TBR1 signal across WT replicates.

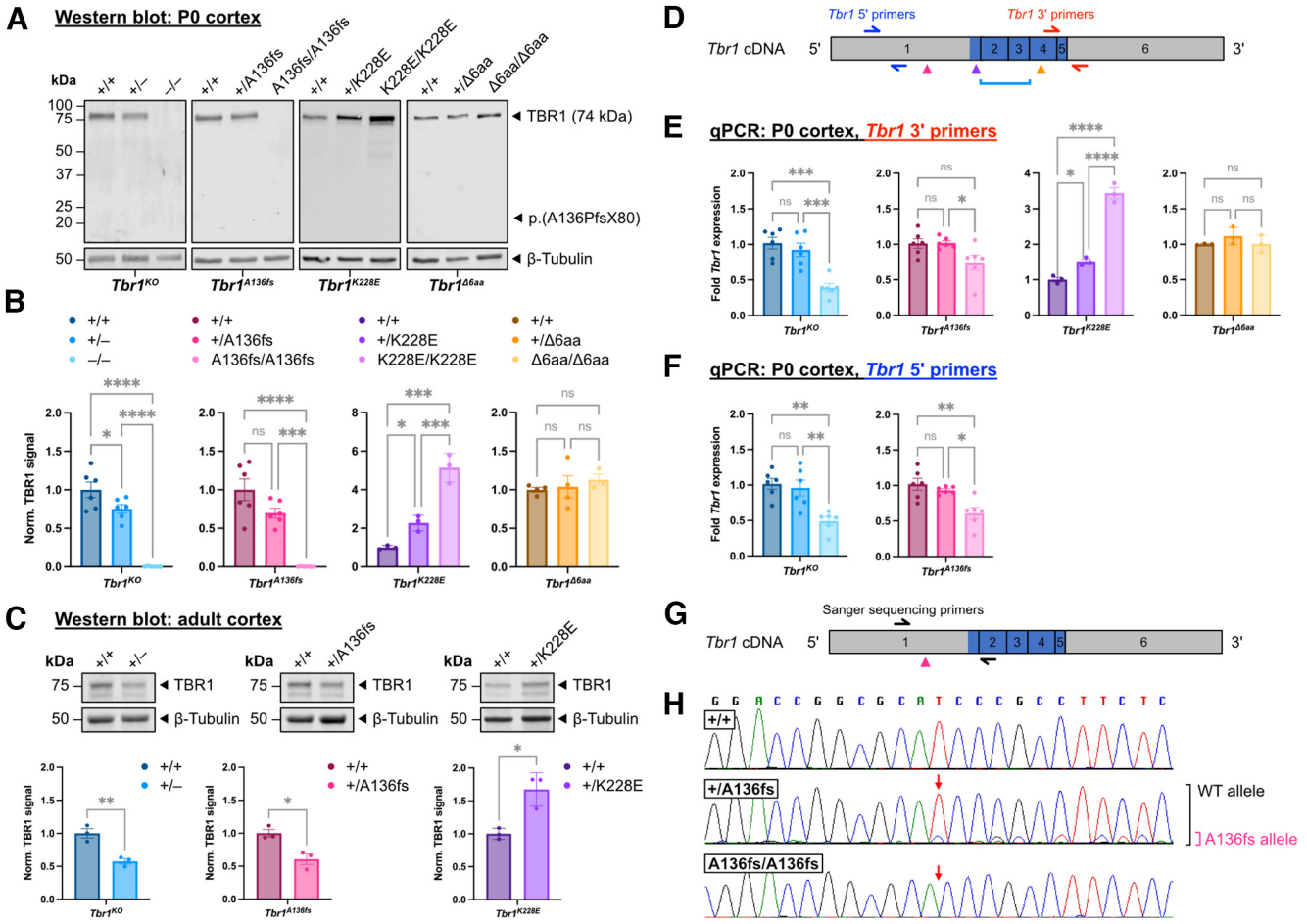

Figure 2. *Tbr1* A136PfsX80 is a loss-of-function mutation, while K228E mutation causes TBR1 upregulation. ***A***, ***B***, Western blots for TBR1 in P0 cortical lysates from *Tbr1* mutant mouse lines ($n = 3$–6 mice/genotype). β-III-Tubulin was used as loading control. Predicted molecular weight of truncated TBR1-A136PfsX80 protein is indicated but not detectable in $Tbr1^{A136fs}$ mutants. ***C***, Western blots for TBR1 in adult cortical lysates from $Tbr1^{KO}$ and patient mutant lines ($n = 3$ mice per genotype). ***D***, Schematic of *Tbr1* cDNA indicating locations of *Tbr1* mutations (arrowheads or bracket) and qPCR primers. Mutations are color-coded as in ***B***. Blue shading indicates T-box coding region. See Extended Data Figure 1-2 for qPCR primer sequences. ***E***, ***F***, qPCR for *Tbr1* using two primer sets in P0 *Tbr1* mutant mouse line cortex ($n = 3$–6 mice per genotype). Genotypes are color coded as in ***B***. ***G***, ***H***, Sanger sequencing of *Tbr1* cDNA from P0 $Tbr1^{A136fs}$ mutant cortex. Red arrows indicate the position of mutation. Brackets indicate peaks corresponding to WT (black) and mutant (magenta) allele in $Tbr1^{+/A136fs}$ cDNA. Data are plotted as the mean ± SEM. Each dot represents one animal. One-way ANOVA with Tukey's multiple-comparisons test was used in ***B***, ***E***, and ***F***; unpaired Student's *t* test was used in ***C***. *$p < 0.05$; **$p < 0.01$; ***$p < 0.001$; ****$p < 0.0001$. ns, Not significant.

Reverse transcription qPCR. Cortex was dissected at P0, flash frozen, and stored at −80°C until all samples were collected. Frozen tissue from one cortical hemisphere (~30 g) was lysed in 1 ml TRIzol Reagent (Thermo Fisher Scientific) and homogenized by passing through a 25 ga needle. Total RNA was extracted using the RNeasy Lipid Tissue Mini Kit (catalog #74804, QIAGEN) with on-column DNase digestion with RNase-Free DNase Set (catalog #79254, QIAGEN) according to the manufacturer protocols. cDNA was synthesized from 1 µg of total RNA using the ProtoScript II First Strand cDNA Synthesis Kit (catalog #E6560S, New England Biolabs) with oligo-dT priming according to the manufacturer protocol. cDNA templates and no RT controls were diluted 1:20 for multiplexed PrimeTime qPCR Assays using *Tbr1* and *Actb* primers with FAM- and SUN-labeled probes, respectively (Integrated DNA Technologies). qPCR assays were run in duplicate or triplicate. Probe fluorescence was measured with a CFX Connect Real-Time PCR Detection System using CFX Manager Software (BIO-RAD) running the following cycling program: 95°C for 3 min, 40 cycles of 95°C for 15 s and 60°C for 1 min, and 4°C hold. qPCR primer efficiencies were measured using WT cortex cDNA for the standard curve (undiluted to 1:10,000) and fell within 90–110%. Ct values were obtained using the "single threshold" Cq Determination Mode in CFX Manager Software (BIO-RAD). After averaging across technical replicates for each sample, *Tbr1* fold gene expression was calculated using the $2^{-\Delta\Delta Ct}$ method with *Actb* as the reference gene and adjustment to the WT average within the respective experimental batch of each sample. For Sanger sequencing of $Tbr1^{A136fs}$ cortex cDNA, 1 µl of cDNA was used as the PCR template for M13 sequence-containing primers spanning exons 1 and 2, and purified PCR product was Sanger sequenced using M13-forward primer. Sanger sequencing traces were visualized using Sequencher software (Gene Codes Corporation; Extended Data Fig. 1-2, primer sequences).

Immunohistochemistry. For P0 samples, whole brains were drop fixed in 4% electron microscopy (EM)-grade paraformaldehyde (PFA) overnight at 4°C, then washed in PBS. For adult samples (9–19 weeks), brains were fixed via transcardial perfusion with 10 ml of PBS and 10 ml of 4% PFA, followed by postfix in 4% PFA for 1 h at 4°C, followed by PBS wash. For cortical layering, interneuron, axon, and apoptosis marker immunohistochemistry (IHC), brains were embedded in 3% low-melting point (LMP) agarose and sectioned coronally or horizontally at 100 µm using a vibratome (model VT1200 S, Leica). Free-floating sections anterior to the hippocampus were incubated in primary antibodies in block solution (2% normal donkey serum, 0.2% Triton X-100 in PBS) for 48–72 h at 4°C, washed in PBS for ≥5 h, incubated in secondary antibodies and Hoechst stain 1:5000 in block solution overnight at 4°C, washed in PBS for ≥5 h, mounted onto glass slides, and coverslipped with Fluoromount-G (Southern Biotech). For TBR1/NeuN IHC in $Tbr1^{K228E}$ cortex, fixed brains were cryoprotected in 30% sucrose overnight at 4°C, washed in PBS, embedded in O.C.T. (optimal cutting

temperature) Compound (Tissue-Tek), and sectioned coronally at 20 µm using a cryostat (model TN50, Tanner). Free-floating cryosections were incubated in primary antibodies in block solution overnight at 4°C, washed in PBS three times for 10 min each, incubated in secondary antibodies and Hoechst stain 1:5000 in block solution for 1 h at room temperature, washed in PBS three times for 10 min each, mounted onto glass slides, and coverslipped with Fluoromount-G (Southern Biotech). The following primary antibodies and dilutions were used: rabbit anti-cleaved caspase-3 (CC3; 1:500; model 9661, Cell Signaling Technology); rat anti-CTIP2 (1:500; catalog #ab18465, Abcam); rabbit anti-CDP/CUX1 (1:500; catalog #sc-13 024, Santa Cruz Biotechnology); rat anti-L1 (1:500; catalog #MAB5272, Millipore); mouse anti-NeuN (1:500; catalog #ab104224, Abcam); mouse anti-neurofilament/neurofilament M (NF-M; 1:500; catalog #2H3, Developmental Studies Hybridoma Bank); goat anti-parvalbumin (1:2000; catalog #PVG-213, Swant); rabbit anti-somatostatin (SST; 1:500; catalog #T-4103.0050, Peninsula Laboratories); and rabbit anti-TBR1 (1:500; catalog #AB10554, Millipore). The following secondary antibodies and dilutions were used: donkey anti-mouse IgG (H + L) Alexa Fluor 488 (1:500; catalog #A-21202, Thermo Fisher Scientific); donkey anti-rabbit IgG (H + L) Alexa Fluor 546 (1:500; catalog #A10040, Thermo Fisher Scientific); donkey anti-goat IgG (H + L) Alexa Fluor 647 (1:500; catalog #A-21447, Thermo Fisher Scientific); and donkey anti-rat IgG (H + L) Alexa Fluor 647 (1:500; catalog #712–605-153, Jackson ImmunoResearch).

Neonatal weight and motor assessments. Weight measurements and negative geotaxis testing were performed at P4, P7, P10, and P14 as previously described (Hill et al., 2008). For negative geotaxis, each pup was placed with its head pointing downward on a 45° incline, and the latency for the pup to face upward on the incline was recorded. If the pup failed to turn within 60 s, or if the pup fell down the incline three times, the latency was recorded as 60 s.

DiI labeling. P0 whole brains were drop-fixed in 4% EM-grade PFA for at least 24 h at 4°C, then washed in PBS. For corticothalamic labeling, DiI crystals (catalog #D3911, Thermo Fisher Scientific) were embedded in primary somatosensory (S1) cortex along the anteroposterior axis. For thalamocortical labeling, DiI crystals were embedded in thalamus after removal of hindbrain. Labeled brains were incubated in 4% PFA at 37°C until labeling was visible in the target brain regions or axon tracts (~9 d). Brains were embedded in 3% LMP agarose and sectioned coronally at 150 µm using a vibratome (model VT1200 S, Leica). Sections were stained with Hoechst 1:5000 in PBS for 10 min, mounted onto glass slides, and coverslipped with Fluoromount-G (Southern Biotech).

Fluorescence image acquisition. Images were acquired using ZEN Blue software (Zeiss). IHC sections were imaged on an upright microscope (model Axio Imager M2, Zeiss) equipped with an ApoTome2. For cortical layering, interneuron, and apoptosis IHC, *z*-stacks were obtained through the tissue section using the optimal interval for each objective. For axon IHC, images were obtained using Tile Scan mode and stitched using ZEN. DiI-labeled sections were imaged on a dissecting microscope (model Axio Zoom.V16, Zeiss).

Cortical layering analysis. Cortical layering analyses were performed on *z*-projection images of coronal sections using ImageJ2/FIJI software. Equivalent background subtraction and brightness/contrast adjustments were applied to all images within an experiment. Images were rotated until layers in S1 were approximately horizontal, then a 1024 × 1800 pixel rectangle was drawn over S1 and rescaled to encompass layer 1 through subplate. Pixel intensities were averaged horizontally within the rectangular selection using "Analyze > Plot Profile," and then these values were averaged into 100 equal bins from layer 1 through subplate (percentage of cortical distance). Binned values for each sample were minimum–maximum normalized using the minimum and maximum average bin values across WT replicates. For the binning of "percentage of cortical distance" into layers for CTIP2 fluorescence comparisons, the following bins were determined based on Hoechst fluorescence: L6, 0–35%; L5, 36–55%; L2–4, 56–100%.

Interneuron distribution analysis. Interneuron distribution analyses were performed on *z*-projection images of coronal sections using ImageJ2/FIJI software. Equivalent background subtraction and binary thresholds were applied to all images within an experiment. Images were rotated until layers in S1 were approximately horizontal, then a rectangular region of interest (ROI) measuring a width of 1024 pixels × height measure in pixels of layer 1 through subplate was drawn over S1. Within this ROI, interneuron counts and *x*–*y* coordinates were obtained using "Measure > Analyze Particles" with equivalent particle size parameters for all images. These values were then used to determine the number of cells per ROI, the fraction of cells per bin (10 bins or 2 bins), and the cumulative density of cells along the ROI.

Apoptosis analysis. Apoptosis analyses were performed on *z*-projection images of coronal sections using ImageJ2/FIJI software. Cells within one cortical hemisphere of one section per animal were manually counted using "Plugins > Analyze > Cell Counter." Cortical area was calculated using the Polygon tool to manually select the ROI.

Results

Generation of *Tbr1* mutant mouse lines

Using CRISPR/Cas9 genome editing (Aida et al., 2015), we generated the following three *Tbr1* mouse lines: $Tbr1^{A136fs}$ (c.402del; p.A136PfsX80), $Tbr1^{K228E}$ (c.682A>G; p.K228E), and $Tbr1^{\Delta 6aa}$ (c.1042_1059del; p.E348_P353del; Fig. 1*A*). The sequence changes producing these predicted mutant proteins are identical between human and mouse. A136PfsX80 is an autism-associated frameshift mutation predicted to yield a truncated protein missing the T-box DNA-binding domain, while K228E is an autism-associated missense mutation within the T-box (O'Roak et al., 2012a,b). Both mutations impact highly conserved residues among vertebrates, and the residues following the frameshift of A136fs are conserved between human and mouse (Fig. 1*B*,*C*). The in-frame deletion mutant p.E348_P353del (Δ6aa) was generated through chance nonhomologous end joining during CRISPR editing intended to generate a different point mutation. This deletion is also located within the T-box and encompasses the following five reported human *TBR1* variants in ClinVar and gnomAD: two nonsense mutations classified as pathogenic or likely pathogenic (S351X, Q352X); and three missense mutations of uncertain or conflicting significance (T350A, S351R, P353A; Extended Data Fig. 1-1; Landrum et al., 2018; Karczewski et al., 2020). Despite strong species conservation of residues 348–353, these residues fall within a poorly conserved site among mouse T-box family proteins (Fig. 1*B*,*D*).

For each line, we tested multiple CRISPR sgRNA sequences, and for $Tbr1^{A136fs}$ and $Tbr1^{K228E}$ we designed single-stranded oligo DNA donors to knock in the mutations through homology-directed repair (Extended Data Fig. 1-2). Using Sanger sequencing, we confirmed the *Tbr1* patient mutations and lack of local (~300 bp) off-target edits in the founder mice (F0) and their offspring (Fig. 1*E*). While the sgRNAs had limited potential for exonic off-target effects (two or fewer off-target mismatches), we further accounted for any off-target edits by backcrossing each line to the parental C57BL/6NJ strain for at least two generations and always comparing littermate controls and mutants within experiments. For $Tbr1^{A136fs}$, we also characterized three separate F1-descendant branches and identified no brain phenotypic differences among these lineages, further suggesting that any phenotypes observed were specific to the primary *Tbr1* editing event.

Heterozygous mutants from the $Tbr1^{A136fs}$, $Tbr1^{K228E}$, and $Tbr1^{\Delta 6aa}$ lines, as well as $Tbr1^{\Delta 6aa}$ homozygotes, appeared healthy with normal outward morphology. In contrast, $Tbr1^{A136fs/A136fs}$ and $Tbr1^{K228E/K228E}$ mice died perinatally and had small olfactory bulbs (Fig. 1*F*). Underdevelopment of the olfactory bulbs was previously described in homozygous mutants from the *Tbr1* knockout ($Tbr1^{KO}$) line, which was generated by replacement of exons 2-3 with a PGK-neomycin cassette (Fig. 1*A*; Bulfone et al., 1998).

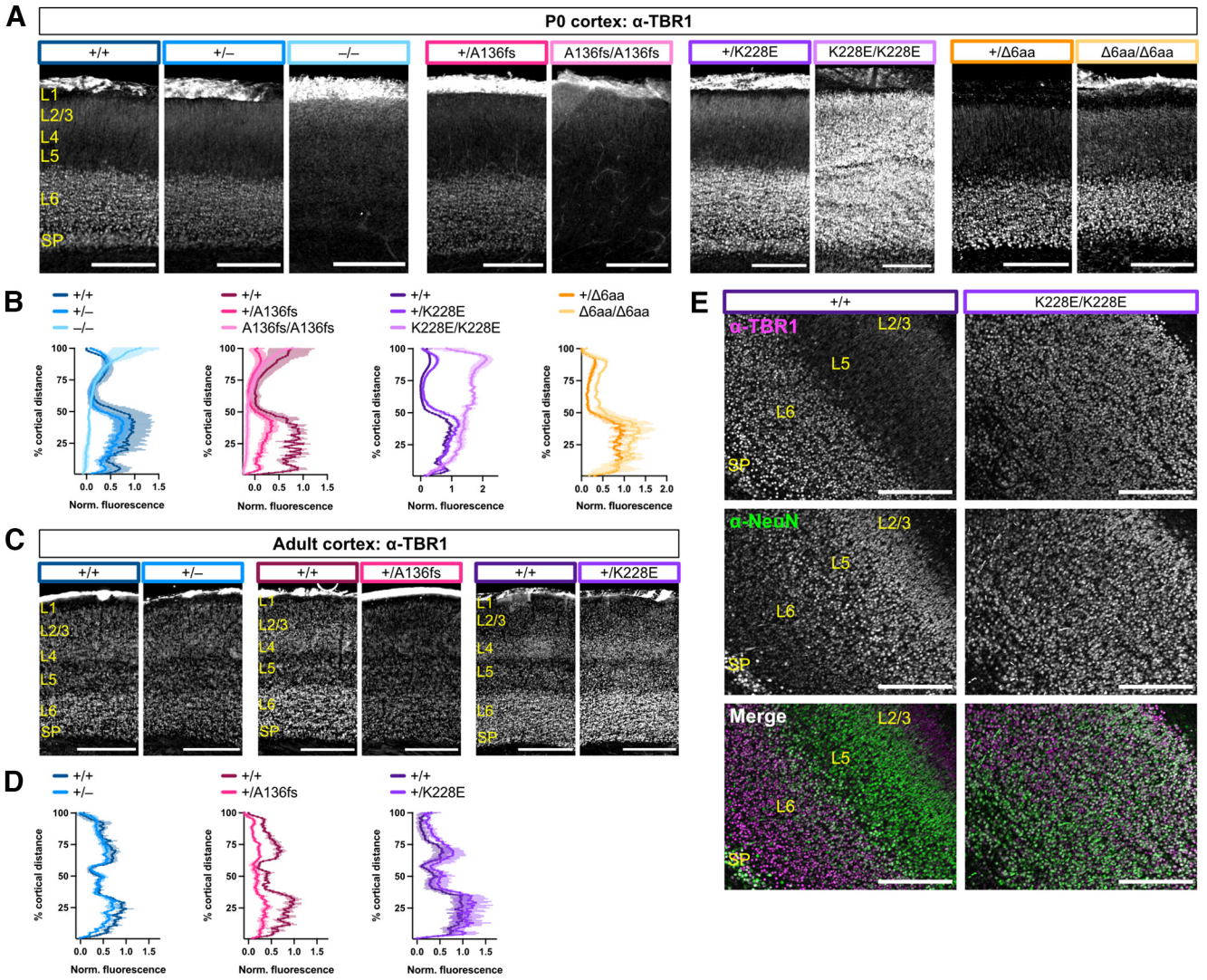

Figure 3. Homozygous K228E mutation causes ectopic TBR1 localization in cortex. ***A***, TBR1 immunostaining in P0 *Tbr1* mutant mouse line S1 cortex. ***B***, Quantification of TBR1 fluorescence intensity across the cortical mantle from ***A*** ($n = 2$–4 mice/genotype). ***C***, ***D***, TBR1 immunostaining and quantification in adult $Tbr1^{KO}$ and patient mutant line S1 cortex. ***E***, Coimmunostaining for TBR1 and NeuN in P0 $Tbr1^{+/+}$ and $Tbr1^{K228E/K228E}$ S1 cortex. SP, Subplate. Scale bars: ***A***, ***E***, 200 μm; ***C***, 500 μm. Data are plotted as the mean ± SEM.

We proceeded to characterize *Tbr1* expression in the $Tbr1^{A136fs}$, $Tbr1^{K228E}$, and $Tbr1^{\Delta 6aa}$ lines in comparison with the $Tbr1^{KO}$ line.

Contrasting effects of *Tbr1* mutations on TBR1 protein levels in cortex

We first measured TBR1 protein levels in P0 cortex from $Tbr1^{KO}$ mice (heterozygotes denoted as $Tbr1^{+/-}$, homozygotes denoted as $Tbr1^{-/-}$) and the CRISPR-generated mutant mouse lines. Full-length TBR1 signal was reduced by ~25% in both $Tbr1^{+/-}$ and $Tbr1^{+/A136fs}$ and completely absent in both $Tbr1^{-/-}$ and $Tbr1^{A136fs/A136fs}$ ($Tbr1^{KO}$: $F_{(2,15)} = 60.2$, $p < 0.001$; $Tbr1^{A136fs}$: $F_{(2,15)} = 33.0$, $p < 0.001$; ANOVA; Fig. 2*A*,*B*). The predicted truncated TBR1-A136PfsX80 protein was also undetectable using an N-terminal TBR1 antibody. In contrast, TBR1 levels were increased by twofold and fivefold in $Tbr1^{+/K228E}$ and $Tbr1^{K228E/K228E}$ cortices, respectively, while TBR1 was unchanged in $Tbr1^{\Delta 6aa}$ mutants ($Tbr1^{K228E}$: $F_{(2,6)} = 55.0$, $p = 0.001$; $Tbr1^{\Delta 6aa}$: $F_{(2,8)} = 0.414$, $p = 0.674$; ANOVA). These TBR1 alterations were maintained in adult heterozygous mutant cortex ($Tbr1^{KO}$, $p = 0.007$; $Tbr1^{A136fs}$, $p = 0.016$; $Tbr1^{K228E}$, $p = 0.012$; *t* test; Fig. 2*C*). Despite decreases in TBR1 protein in $Tbr1^{KO}$ and $Tbr1^{A136fs}$ mutants, qPCR analysis using primers downstream of these mutations revealed that *Tbr1* transcript levels were not decreased in heterozygotes, and were modestly decreased in homozygotes, suggesting that the protein reductions resulted from post-transcriptional processes ($Tbr1^{KO}$: $F_{(2,15)} = 18.4$, $p < 0.001$; $Tbr1^{A136fs}$: $F_{(2,15)} = 4.45$, $p = 0.030$; ANOVA; Fig. 2*D*,*E*). To validate this finding and compare transcript degradation at the 5′ end versus the 3′ end of mutant transcripts, we repeated qPCR with primers targeting the 5′ end of *Tbr1* and obtained similar results as the 3′ qPCR ($Tbr1^{KO}$: $F_{(2,15)} = 11.4$, $p = 0.001$; $Tbr1^{A136fs}$: $F_{(2,15)} = 10.1$, $p = 0.002$; ANOVA; Fig. 2*D*,*F*). However, when we performed Sanger sequencing of cDNA from $Tbr1^{+/A136fs}$ cortex, transcripts from the mutant allele comprised only a small proportion of the overall *Tbr1* transcript, suggesting upregulation from the WT allele and/or degradation of mutant transcripts via nonsense-mediated decay or other mRNA surveillance mechanisms (Fig. 2*G*, *H*). In $Tbr1^{+/K228E}$, and $Tbr1^{K228E/K228E}$, *Tbr1* was increased by 1.5-fold and 3.5-fold, respectively, indicating that their increased TBR1 protein levels are attributable to transcriptional upregulation ($Tbr1^{K228E}$: $F_{(2,6)} = 156.6$, $p < 0.001$; ANOVA; Fig. 2*E*). *Tbr1* transcript levels were unchanged in $Tbr1^{\Delta 6aa}$ mutants ($Tbr1^{\Delta 6aa}$: $F_{(2,8)} = 1.31$, $p = 0.337$; ANOVA; Fig. 2*E*).

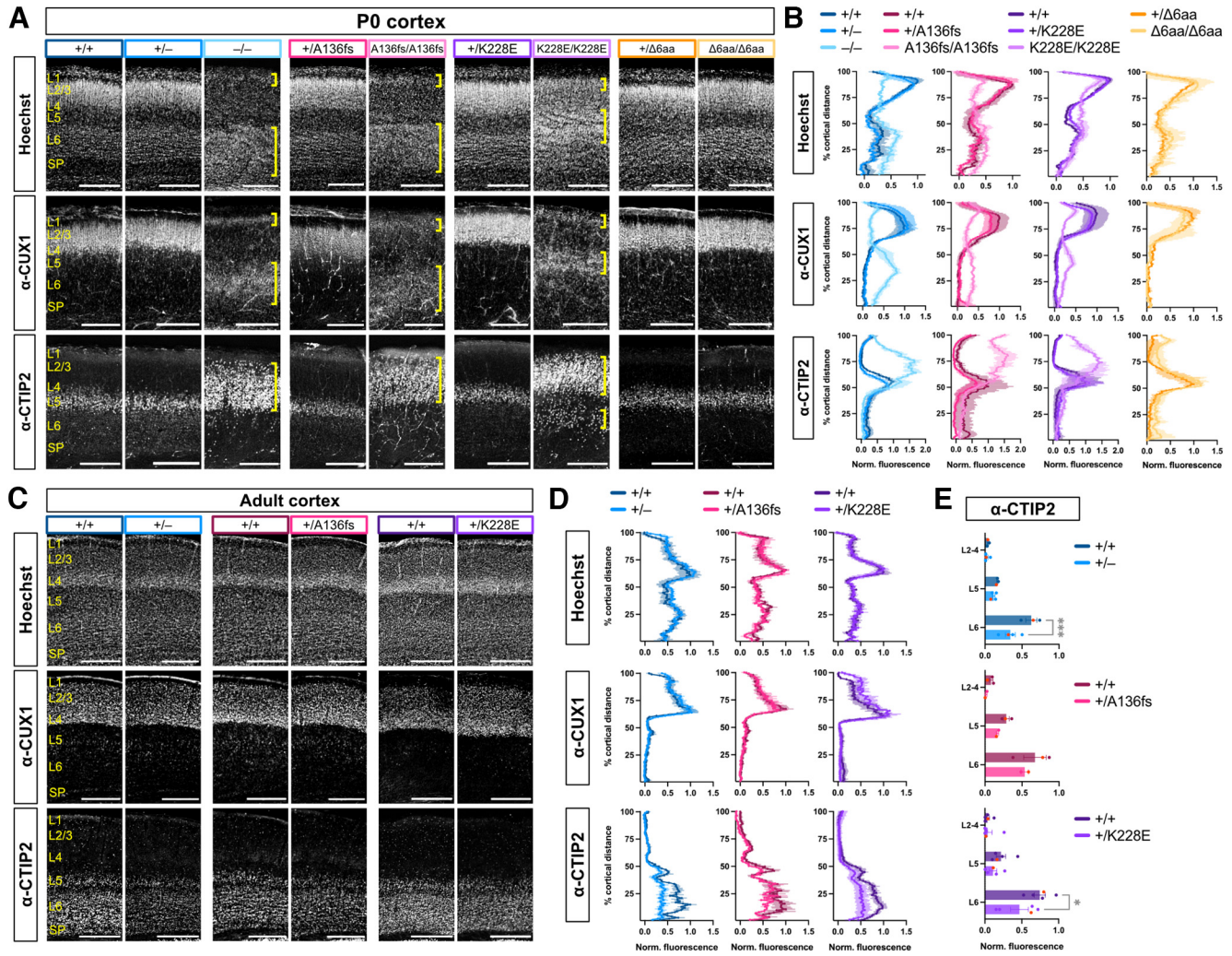

Figure 4. K228E mutation causes distinct cortical layering defects from *Tbr1* knockout and A136PfsX80. ***A***, Hoechst nuclear stain and immunostaining for cortical layer markers CUX1 (L2–4) and CTIP2 (L5) in P0 *Tbr1* mutant mouse line S1 cortex. Yellow brackets indicate abnormal cortical layers formed in homozygous mutants. ***B***, Quantification of Hoechst, CUX1, and CTIP2 fluorescence intensity across the cortical mantle from ***A*** ($n = 2$–4 mice/genotype). ***C***, ***D***, Hoechst, CUX1, and CTIP2 staining and quantification in adult $Tbr1^{KO}$ and patient line S1 cortex ($n = 2$–4 mice/genotype). ***E***, CTIP2 fluorescence binned by cortical layers using fluorescence values from ***D***. SP, Subplate. Scale bars: ***A***, 200 μm; ***C***, 500 μm. Data are plotted as the mean ± SEM. Each dot represents one animal; red dots correspond to representative images. Two-way ANOVA with Šídák's multiple-comparisons test was used in ***E***. $^{*}p < 0.05$; $^{***}p < 0.001$.

In the developing cortex, TBR1 is present at high levels in deep-layer excitatory projection neurons, and in adulthood is present in both upper-layer and deep-layer excitatory neurons (Hevner et al., 2001). To assess TBR1 layer distribution and levels, we immunostained for TBR1 in P0 and adult brain sections and plotted fluorescence profiles across the cortical layers. At both neonatal and adult stages, heterozygotes of each mutant line showed TBR1 layer distributions similar to those of WT (Fig. 3*A*–*D*). While $Tbr1^{-/-}$ and $Tbr1^{A136fs/A136fs}$ showed minimal TBR1 fluorescence at P0, $Tbr1^{K228E/K228E}$ unexpectedly showed substantial TBR1 upregulation across all cortical layers (Fig. 3*A*, *B*). In these mice, the vast majority of $NeuN^{+}$ cortical neurons expressed TBR1 (Fig. 3*E*). In contrast to the other homozygous mutants, $Tbr1^{\Delta 6aa/\Delta 6aa}$ showed normal deep-layer TBR1 expression in P0 cortex (Fig. 3*A*,*B*). Overall, these results show the following: (1) A136PfsX80 causes the absence of TBR1 protein; (2) K228E causes elevated TBR1 levels because of transcriptional upregulation and, in homozygotes, ectopic protein expression; and (3) the deletion of residues 348–353 has no impact on TBR1 levels.

Homozygosity of different *Tbr1* mutations causes distinct cortical layering phenotypes

During corticogenesis, newborn neurons migrate outward from a germinal zone to form six cytoarchitectural layers, and neuronal subpopulations within each layer obtain distinct transcriptional and functional identities (Kwan et al., 2012). $Tbr1^{-/-}$ mice show *reeler*-like disorganization of cortical layering and misspecification of layer 6 (L6) neurons to L5-like neurons (Hevner et al., 2001; Han et al., 2011; McKenna et al., 2011). To examine cortical formation and neuronal identity in the *Tbr1* mutant lines, we immunostained for layer markers CUX1 (L2–4) and CTIP2 (L5) and costained for nuclear marker Hoechst at P0 and adulthood. At both stages, all *Tbr1* heterozygotes and $Tbr1^{\Delta 6aa/\Delta 6aa}$ homozygotes showed grossly normal layer formation in primary somatosensory (S1) cortex (Fig. 4*A*–*D*). By adulthood, $Tbr1^{+/-}$, $Tbr1^{+/A136fs}$, and $Tbr1^{+/K228E}$ heterozygotes showed reductions in CTIP2 fluorescence intensity in L6, suggesting downregulation of this transcription factor in mature heterozygous mutant cortex ($Tbr1^{KO}$: $F_{(1,15)} = 11.1$, $p = 0.005$; $Tbr1^{A136fs}$: $F_{(1,9)} = 2.44$, $p = 0.153$; $Tbr1^{K228E}$:

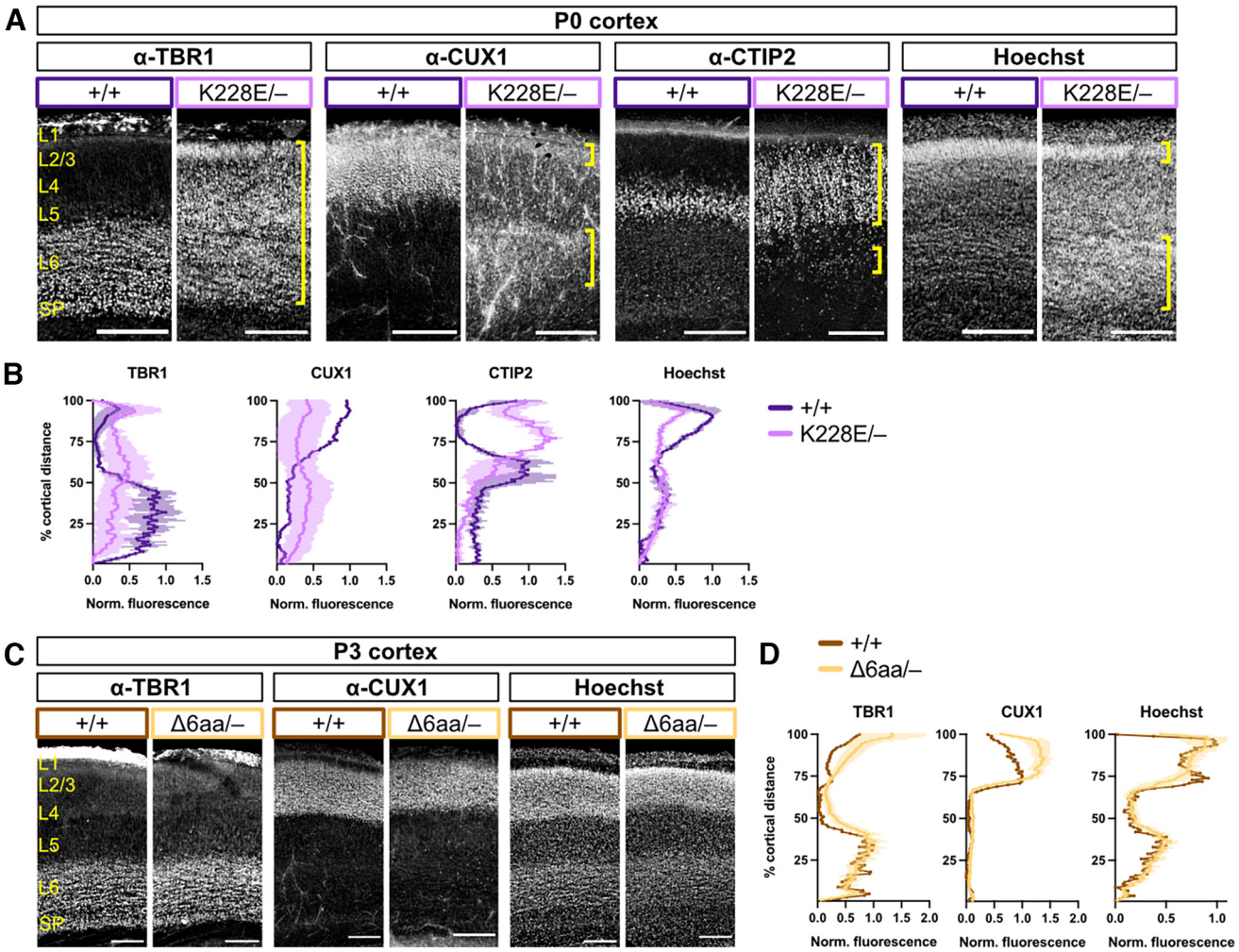

Figure 5. Complementation cross shows limited functionality of K228E allele. ***A***, TBR1, CUX1, and CTIP2 immunostaining and Hoechst nuclear stain in S1 cortex of P0 offspring from $Tbr1^{KO}$ and $Tbr1^{K228E}$ complementation cross. Yellow brackets indicate abnormal cortical layers formed in $Tbr1^{K228E/-}$ mice. ***B***, Quantification of TBR1, CUX1, CTIP2, and Hoechst fluorescence intensity across the cortical mantle from ***A*** ($n = 1$–2 mice/genotype). ***C***, ***D***, TBR1, CUX1, and Hoechst staining and fluorescence quantification in S1 cortex of P3 offspring from $Tbr1^{KO}$ and $Tbr1^{\Delta 6aa}$ complementation cross ($n = 1$–5 mice/genotype). SP, Subplate. Scale bars: ***A*** and ***C***, 200 μm. Data are plotted as the mean ± SEM.

$F_{(1,24)} = 4.84$, $p = 0.038$; ANOVA; Fig. 4*C*,*E*). Homozygous $Tbr1^{-/-}$, $Tbr1^{A136fs/A136fs}$, and $Tbr1^{K228E/K228E}$ mice showed major cortical layering defects differing by mutation (Fig. 4*A*, *B*). Specifically, in $Tbr1^{-/-}$ and $Tbr1^{A136fs/A136fs}$ mice, layer positions were inverted, with $CUX1^+$ cells mostly residing in inner cortex and $CTIP2^+$ cells almost exclusive to outer cortex. In contrast, $Tbr1^{K228E/K228E}$ mice showed a more complex layering phenotype, with $CUX1^+$ cells forming a thin mid-cortical layer and $CTIP2^+$ cells residing in both outer and inner cortex. $Tbr1^{-/-}$, $Tbr1^{A136fs/A136fs}$, and $Tbr1^{K228E/K228E}$ homozygotes also showed an overabundance of $CTIP2^+$ neurons compared with WT, suggesting L6-to-L5 misspecification. Overall, these data indicate that one WT copy of *Tbr1* is sufficient for normal cortical layer formation. Furthermore, KO, A136PfsX80, and K228E mutations have discordant effects on cortical layer formation, but congruent effects on deep-layer marker CTIP2 expression.

To further assess the functionality of the K228E and Δ6aa alleles, we performed genetic complementation tests by crossing each of these mutant lines with the $Tbr1^{KO}$ line. $Tbr1^{K228E/-}$ cortical layering was phenotypically intermediate between $Tbr1^{-/-}$ and $Tbr1^{K228E/K228E}$, with CUX1 and Hoechst distributions resembling the former, and TBR1 and CTIP2 distributions resembling the latter (Fig. 5*A*,*B*). In contrast, $Tbr1^{\Delta 6aa/-}$ mice showed normal layer formation, despite having only one copy of the mutant allele on a null background (Fig. 5*C*,*D*). These results confirm that the T-box mutant K228E has insufficient functionality to mediate proper cortical layer formation, while amino acids 348–353 of the T-box are dispensable for layer formation. Thus, we limited further characterization of the $Tbr1^{\Delta 6aa}$ line to focus on the more pathogenic patient-specific mutations.

Tbr1 mutant mice show normal growth and motor function

Patients with *TBR1* mutations have been reported to exhibit microcephaly, growth delay, developmental motor delay, and hypotonia (Palumbo et al., 2014; Nambot et al., 2020). We assessed postnatal growth in $Tbr1^{KO}$, $Tbr1^{A136fs}$, and $Tbr1^{K228E}$ mutant mice but found no changes in brain-to-body mass ratio at P0 ($Tbr1^{KO}$: $F_{(2,30)} = 2.16$, $p = 0.133$; $Tbr1^{A136fs}$: $F_{(2,18)} = 1.56$, $p = 0.238$; $Tbr1^{K228E}$: $F_{(2,28)} = 0.665$, $p = 0.522$; ANOVA), or in body mass from P4 to P14 ($Tbr1^{KO}$: $F_{(1,22)} = 0.184$, $p = 0.673$; $Tbr1^{A136fs}$: $F_{(1,40)} = 0.941$, $p = 0.338$; $Tbr1^{K228E}$: $F_{(1,23)} = 0.00{,}895$, $p = 0.926$; ANOVA; Fig. 6*A*,*B*). Furthermore, heterozygous mutants did not show impairment in the negative geotaxis motor test across postnatal development ($Tbr1^{KO}$: $F_{(1,14)} = 1.17$, $p = 0.297$;

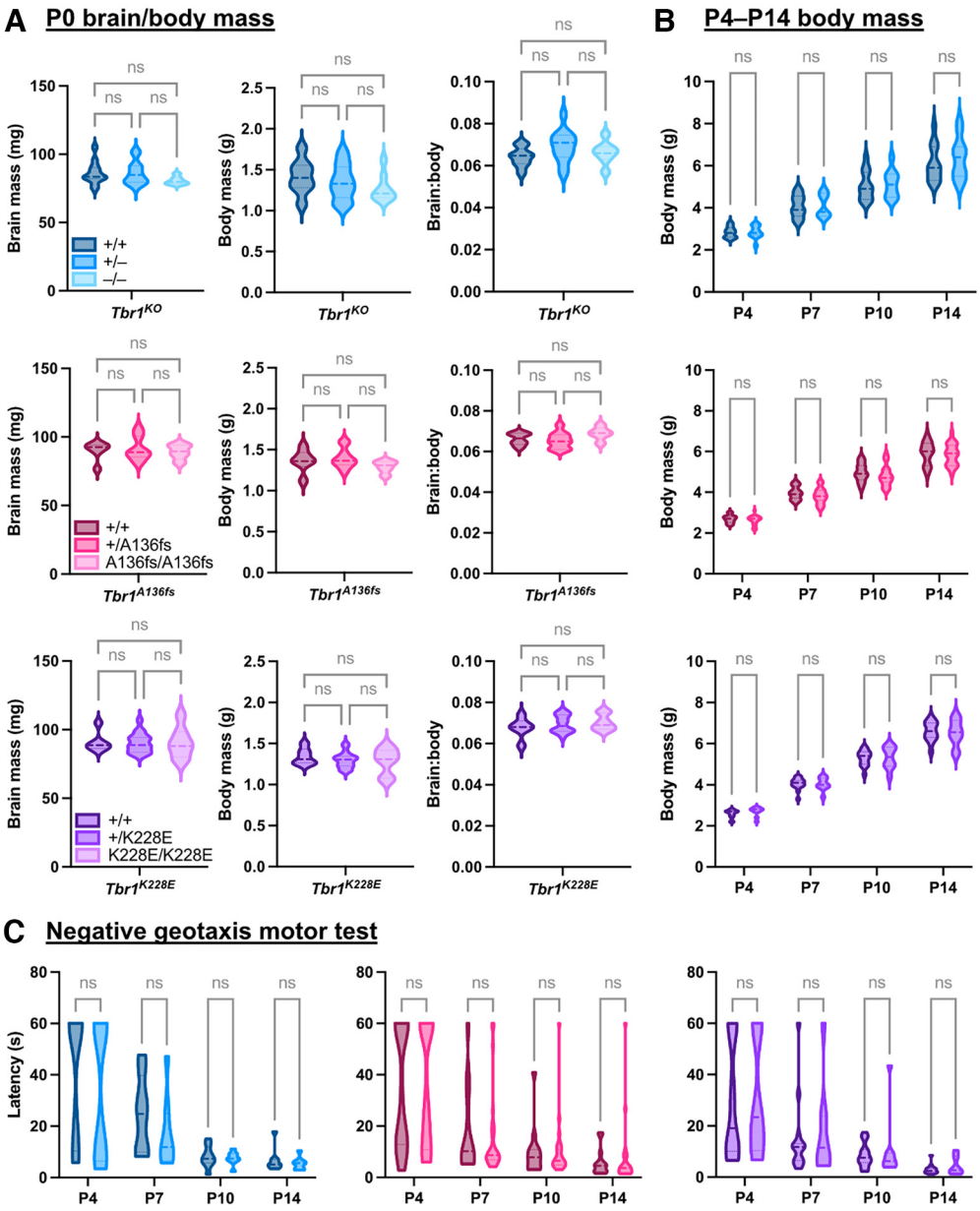

Figure 6. Normal growth and motor development of postnatal *Tbr1* mutant mice. ***A***, Brain mass, body mass, and brain/body mass ratio measurements for $Tbr1^{KO}$ and patient mutant mouse lines at P0 ($n = 5$–18 mice/genotype). ***B***, Body mass measurements for $Tbr1^{KO}$ and patient mutant mouse lines across postnatal development ($n = 10$–27 mice/genotype). ***C***, Latency for mouse pups to orient upward on a slope in the negative geotaxis test of motor coordination ($n = 8$–26 mice/genotype). One-way ANOVA with Tukey's multiple-comparisons test was used in ***A***; two-way repeated-measures ANOVA with Šídák's multiple-comparisons test was used in ***B*** and ***C***. ns, Not significant.

$Tbr1^{A136fs}$: $F_{(1,39)} = 7.76\text{e-}005$, $p = 0.993$; $Tbr1^{K228E}$: $F_{(1,22)} = 0.305$, $p = 0.586$; ANOVA; Fig. 6*C*). Thus, these *Tbr1* mutations have minimal impact on the growth and gross motor function of mice during development.

Tbr1 mutant mice show normal interneuron distributions in S1 cortex

While *Tbr1* expression in the cortex is restricted to glutamatergic neurons, $Tbr1^{-/-}$ mice show abnormal distribution of GABAergic interneurons; furthermore, $Tbr1^{+/K228E}$ mice show displacement of PV-expressing interneurons, but not other interneuron subtypes, in medial prefrontal cortex (Hevner et al., 2001; Yook et al., 2019). To examine non-cell-autonomous effects of *Tbr1* mutations on cortical interneuron distribution, we immunostained for the major interneuron subtype markers PV and SST in S1 cortex of adult $Tbr1^{+/-}$, $Tbr1^{+/A136fs}$, and $Tbr1^{+/K228E}$ mice (Fig. 7*A*,*B*). For each interneuron subtype, we found no changes in cell density (SST $Tbr1^{KO}$, $p = 0.293$; SST $Tbr1^{A136fs}$, $p = 0.318$; SST $Tbr1^{K228E}$, $p = 0.897$; PV $Tbr1^{KO}$, $p = 0.821$; PV $Tbr1^{A136fs}$, $p = 0.902$; PV $Tbr1^{K228E}$, $p = 0.459$; *t* test) or distribution (SST $Tbr1^{KO}$, $p = 0.994$; SST $Tbr1^{A136fs}$, $p > 0.999$; SST $Tbr1^{K228E}$, $p > 0.999$; PV $Tbr1^{KO}$, $p = 0.699$; PV $Tbr1^{A136fs}$, $p > 0.999$; PV $Tbr1^{K228E}$, $p > 0.999$; Kolmogorov–Smirnov test; Fig. 7*C*–*J*). These results indicate limited impact of *Tbr1* mutations on interneuron distributions in S1 cortex.

Tbr1 patient mutations A136fs and K228E cause equivalent axon tract defects to *Tbr1* KO

Tbr1 is required for normal axon tract development in the brain: $Tbr1^{-/-}$ mice show severe defects of the corpus callosum, internal

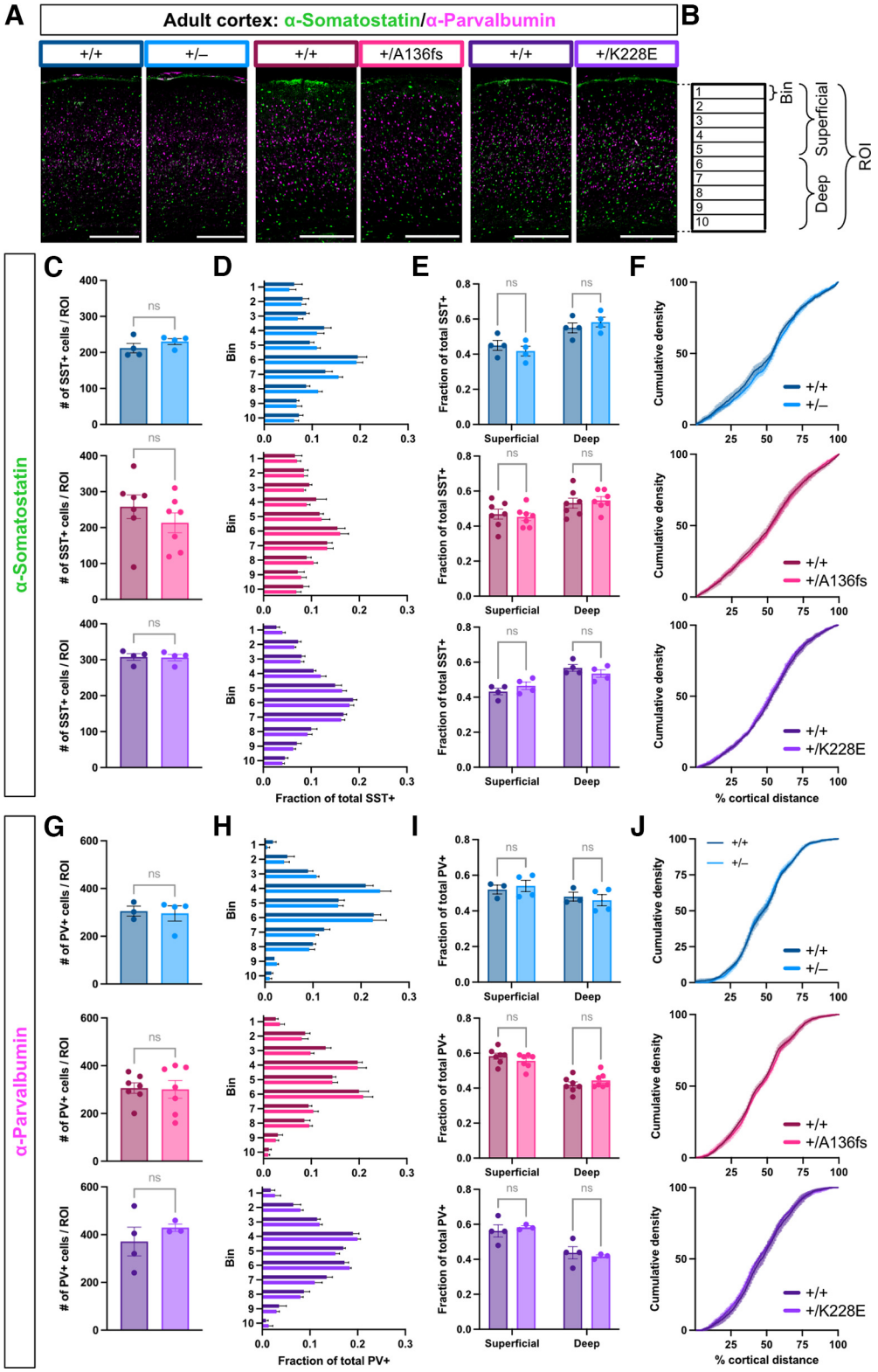

Figure 7. Normal distribution of cortical interneurons in *Tbr1* mutant mice. ***A***, Immunostaining for interneuron subtype markers SST (green) and PV (magenta) in adult *Tbr1*^{KO} and patient mutant line S1 cortex. ***B***, Schematic illustrating bins and ROI for interneuron quantification. ***C***, Number of SST$^+$ cells per ROI ($n = 3$–7 mice/genotype). ***D***, Fraction of SST$^+$ cells distributed across 10 equal-sized bins of ROI. ***E***, Fraction of SST$^+$ cells distributed between superficial (bins 1–5) and deep (bins 6–10) cortex. ***F***, Cumulative density of SST$^+$ cells across the cortical mantle. ***G–J***, Quantification of PV$^+$ cells as in ***B–E*** ($n = 3$–7 mice/genotype). Scale bar: ***A***, 500 μm. Data are plotted as the mean ± SEM. Each dot represents one animal. Unpaired Student's *t* test was used in ***C*** and ***G***; two-way ANOVA with Šídák's multiple-comparisons test was ***D***, ***E***, ***H***, and ***I***; Kolmogorov–Smirnov test was used in ***F*** and ***J***. ns, Not significant.

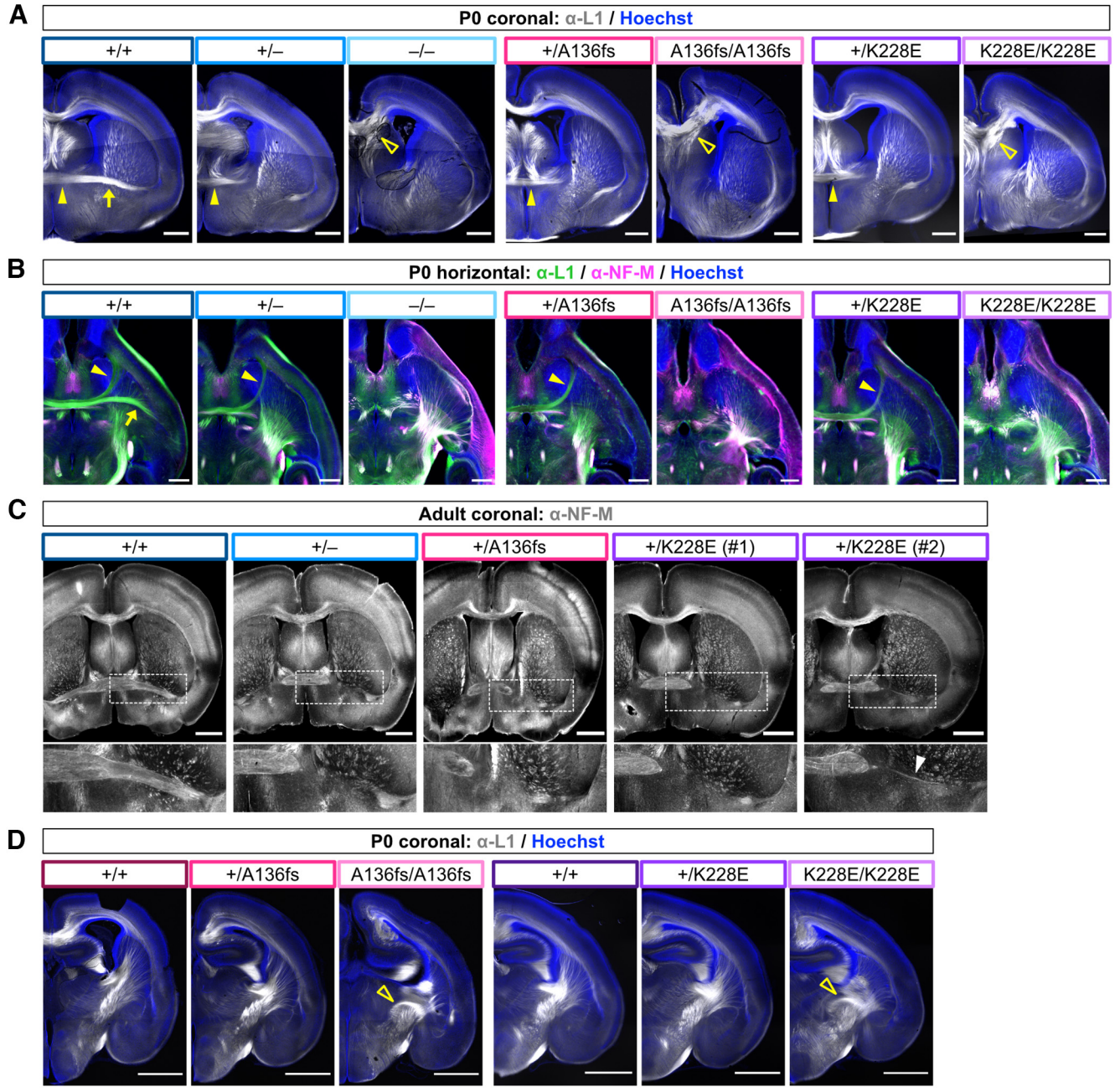

Figure 8. Congruent axon tract defects across *Tbr1* mutant mouse lines. ***A***, Immunostaining for axon marker L1 (white) and Hoechst nuclear stain (blue) in P0 coronal brain sections from $Tbr1^{KO}$ and patient mutant lines. Arrow indicates posterior limb of AC in wild-type mouse. Closed arrowhead indicates anterior limb of AC in wild-type and heterozygous mutant mice. Open arrowheads indicate bundled and misdirected callosal axons in homozygous mutants. $n = 3$–4 mice examined per genotype. ***B***, Immunostaining for L1 (green) and NF-M (magenta) with Hoechst (blue) in P0 horizontal brain sections from $Tbr1^{KO}$ and patient mutant lines. Arrow indicates posterior limb of AC in wild-type mouse. Arrowhead indicates anterior limb of AC in wild-type and heterozygous mutant mice. $n = 2$ mice examined per genotype. ***C***, Immunostaining for NF-M in adult coronal brain sections from $Tbr1^{KO}$ and patient mutant lines. Inset (dotted lines) shows higher magnification of posterior limb of AC. Arrowhead indicates thin AC posterior limb observed in one $Tbr1^{K228E}$ heterozygote. $n = 3$–6 mice examined per genotype. ***D***, Immunostaining for L1 (white) and Hoechst (blue) in P0 coronal brain sections from *Tbr1* patient lines. Arrowheads indicate abnormal organization of internal capsule axons in homozygotes. Scale bars: ***A***, ***B***, 500 μm; ***C***, ***D***, 1 mm.

capsule, and AC, and $Tbr1^{+/-}$ mice lack the posterior limb of the AC (Hevner et al., 2001; Huang et al., 2014). To examine axon tract formation in the *Tbr1* patient mutant lines, we immunostained for axon markers L1 and NF-M at P0 and adulthood. At these stages, nearly all heterozygotes examined from each *Tbr1* line lacked the posterior limb of the AC, indicating a congruent and highly penetrant phenotype of heterozygous *Tbr1* mutation ($Tbr1^{+/-}$, $n = 10$ of 10 missing posterior limb; $Tbr1^{+/A136fs}$, $n = 8$ of 8 missing posterior limb; $Tbr1^{+/K228E}$, $n = 7$ of 8 mice missing posterior limb; Fig. 8*A*–*C*). One adult $Tbr1^{+/K228E}$ mouse showed a very thinly formed posterior limb (Fig. 8*C*, arrowhead). Homozygotes from each *Tbr1* line showed more severe axon defects, including misdirected callosal fibers and complete absence of the AC, as well as aberrant upregulation of NF-M in the cortex (Fig. 8*A*,*B*). We also examined the internal capsule, which contains corticothalamic and thalamocortical axon fibers, and observed grossly normal organization of this tract in heterozygotes and abnormal organization in homozygotes (Fig. 8*D*).

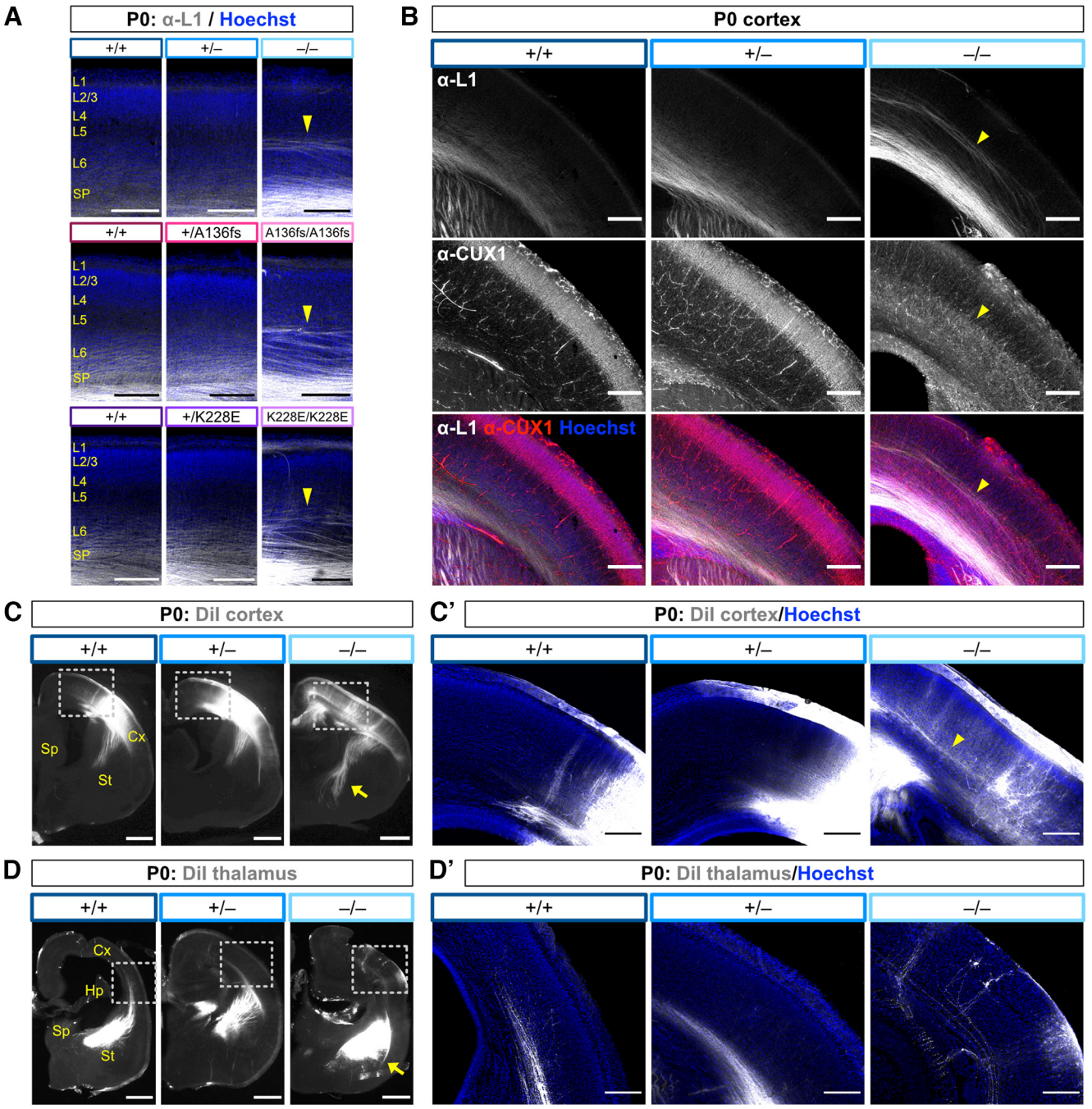

Figure 9. Ectopic axons in *Tbr1* homozygous mutants originate within the cortex. ***A***, Immunostaining for axon marker L1 (white) and Hoechst nuclear stain (blue) in P0 $Tbr1^{KO}$ and patient mutant line S1 cortex. Arrowheads indicate ectopic intracortical axons in homozygotes. ***B***, Immunostaining for L1 (white), CUX1 (red), and Hoechst (blue) in P0 S1 cortex from $Tbr1^{KO}$ line. Arrowheads indicate positioning of ectopic axons at $CUX1^{+}$ layer boundary in homozygous mutants. ***C–C′***, DiI-labeled cortical axons (white) in P0 coronal brain sections from $Tbr1^{KO}$ line. Arrow indicates subcortical axon overgrowth in homozygous mutants. Dotted lines show inset of cortex in ***C′*** with Hoechst counterstain (blue), and arrowhead indicates DiI-labeled cortical axons in homozygous mutant. ***D–D′***, DiI labeled thalamic axons (white) in P0 coronal brain sections from $Tbr1^{KO}$ line. Arrow indicates misrouted thalamic axons in external capsule. Dotted lines show inset of cortex in ***D′*** with Hoechst counterstain (blue). Cx, Cortex; Hp, hippocampus; Sp, septum; St, striatum. Scale bars: ***A***, ***B***, ***C′***, ***D′***, 200 μm; ***C***, ***D***, 500 μm.

In addition to these defects, we identified ectopic L1-labeled axons in the mid-cortex of $Tbr1^{-/-}$, $Tbr1^{A136fs/A136fs}$, and $Tbr1^{K228E/K228E}$ at P0 (Fig. 9*A*). These axons were constrained to the abnormal inner $CUX1^{+}$ cortical layer in $Tbr1^{-/-}$ mice (Fig. 9*B*). Because $Tbr1^{-/-}$ mice lack the subplate layer along which thalamic axons normally travel to innervate the cortex (Hevner et al., 2001), we sought to determine whether these ectopic cortical axons were misguided thalamocortical afferents, or whether they originated intracortically. We placed DiI crystals in either the thalamus or the cortex of P0 brains, and we observed DiI-labeled cortical axons forming a narrow mid-cortical tract similar to the L1-labeled ectopic axons (Fig. 9*B*, *C*). Thalamic axons, on the other hand, were misrouted ventrally into the external capsule and did not enter the cortex (Fig. 9*D*). Altogether, our results show congruent axon defects across $Tbr1^{KO}$ and patient mutant mouse lines, including a newly observed intracortical axon defect in homozygous mutants.

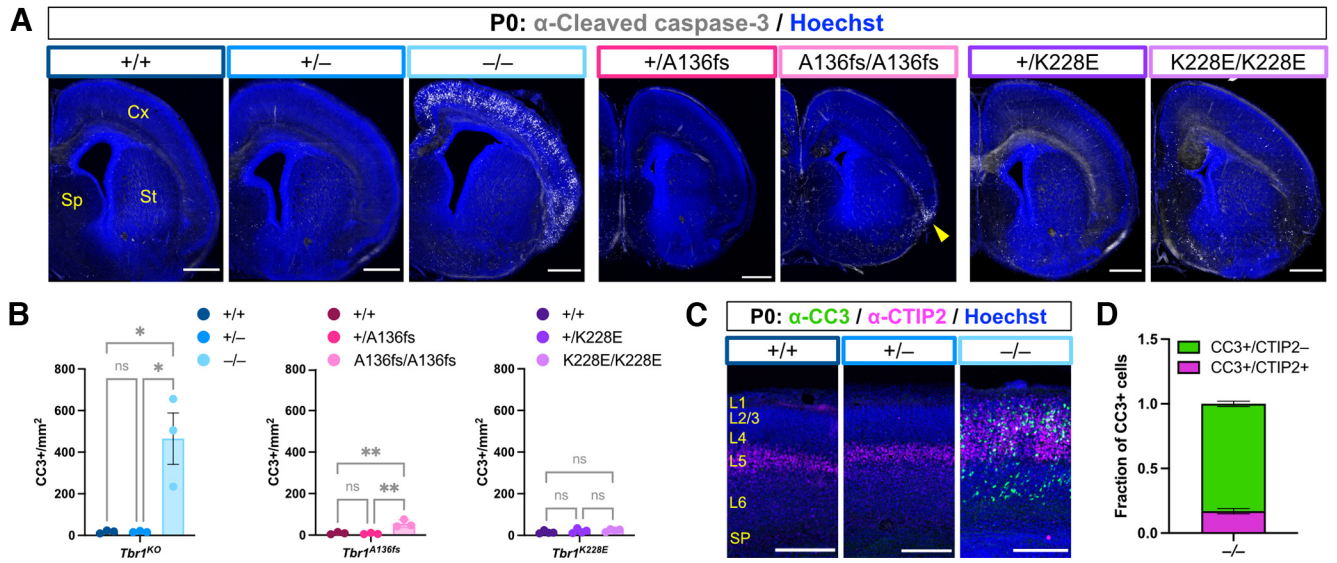

Figure 10. *Tbr1* knock-out mice, but not patient mutant mice, show widespread cortical apoptosis. ***A***, ***B***, Immunostaining and quantification of $CC3^+$ apoptotic cells (white) in P0 cortex from $Tbr1^{KO}$ and patient mutant mouse lines ($n = 3$ mice/genotype). Hoechst nuclear stain is shown in blue. ***C***, ***D***, Immunostaining and quantification of $CC3^+$ apoptotic cells (green) colabeled with CTIP2 (magenta) in cortex of P0 $Tbr1^{-/-}$ mice ($n = 3$). Hoechst stain is shown in blue. Scale bars: ***A***, 500 μm; ***C***, 200 μm. Data are plotted as the mean ± SEM. Each dot represents one animal. One-way ANOVA with Tukey's multiple-comparisons test was used in ***B***. *$p < 0.05$; **$p < 0.01$. ns, Not significant.

Tbr1 KO mice, but not patient mutant mice, show extensive cortical apoptosis

Previous studies of cell survival in $Tbr1^{-/-}$ cortex found a substantial increase in the apoptotic marker CC3 starting by embryonic day 16.5 and continuing to P0 (Bedogni et al., 2010). To examine cortical cell survival in $Tbr1^{KO}$ and patient mutant mice, we immunostained for CC3 at P0. WT and heterozygous mutant mice of each line showed very few $CC3^+$ cells at this time point (Fig. 10*A*,*B*). However, while we saw drastically increased $CC3^+$ cell density in $Tbr1^{-/-}$ cortex, we saw a limited increase of $CC3^+$ cells in $Tbr1^{A136fs/A136fs}$ and no increase in $Tbr1^{K228E/K228E}$ ($Tbr1^{KO}$: $F_{(2,6)} = 13.2$, $p = 0.006$; $Tbr1^{A136fs}$: $F_{(2,6)} = 17.5$, $p = 0.003$; $Tbr1^{K228E}$: $F_{(2,9)} = 1.18$, $p = 0.350$; ANOVA). Furthermore, $CC3^+$ cells in $Tbr1^{-/-}$ cortex spanned multiple cortical areas, while $CC3^+$ cells in $Tbr1^{A136fs/A136fs}$ were restricted to the piriform area (Fig. 10*A*, arrowhead). When we costained for CC3 and L5 marker CTIP2 in $Tbr1^{-/-}$ cortex, we found that $CC3^+$ cells were not confined to the $CTIP2^+$ layer, and that 16.8% of the total $CC3^+$ cells were $CTIP2^+$ (Fig. 10*C*,*D*). Thus, homozygosity of the *Tbr1* exon 2-3 knock-out allele causes widespread cortical apoptosis, while patient mutant alleles A136PfsX80 and K228E have limited impacts on cortical cell survival.

Discussion

In this study, we sought to understand the etiology of *TBR1*-related neurodevelopmental conditions via modeling of patient-specific *de novo* mutations in mice. Comparing directly with $Tbr1^{KO}$ mice previously used to study this transcription factor, we identified a number of shared and distinct phenotypic effects (Fig. 11*A*). The *de novo* frameshift mutant A136PfsX80 (A136fs) generally phenocopied the KO, suggesting that this mutation is loss-of-function, while the *de novo* missense mutant K228E showed cortical disorganization distinct from KO and A136fs. One key difference among all three *Tbr1* mutant lines was the extent of cortical apoptosis, with homozygous KO causing severe apoptosis, A136fs limited apoptosis, and K228E normal apoptosis. In addition to these discordant phenotypes, we found several congruent defects across *Tbr1* lines in olfactory bulb development, axon tract formation, and CTIP2 and NF-M levels. These findings reveal molecular and cellular processes sensitive to *Tbr1* gene disruption regardless of mutation type, suggesting core biomarkers or therapeutic targets for *TBR1*-related conditions. Furthermore, identification of mutation-specific effects may lend insight into the phenotypic variability of these conditions.

Construct validity of *Tbr1* mouse models for neurodevelopmental conditions

Upon the association of *TBR1* mutations with neurodevelopmental conditions, several *Tbr1* mutant mouse models were generated to study their underlying biological mechanisms. Mice with one copy of *Tbr1* disrupted by insertion of a PGK-neo cassette were used to model human *TBR1* haploinsufficiency (Bulfone et al., 1998; Huang et al., 2014). To identify autism-related functions of *Tbr1* within cortical neuron subpopulations, Cre-loxP recombination was used to delete *Tbr1* in layer 5 or layer 6 during late embryonic to early postnatal development (Fazel Darbandi et al., 2018, 2020, 2022). Cre-loxP was also used to generate mice carrying the K228E patient mutation before our study (Yook et al., 2019). While these models have revealed potential molecular and cellular mechanisms underlying *TBR1*-related conditions, their construct validity is limited by the retention of genomic artifacts (i.e., neo cassette, loxP sites) and/or the timing of *Tbr1* deletion several days after its initial expression. With CRISPR genome editing, we addressed these potential limitations in our *Tbr1* models by incorporating the exact patient mutations into the mouse genome without the inclusion of additional sequences.

These differences in mouse line generation methods could explain the phenotypic discrepancies between our CRISPR-generated *Tbr1* models and previous models. For example, the severe cortical apoptosis unique to $Tbr1^{-/-}$ mice (Fig. 10) could potentially result from the production of an aberrant transcript from the neo cassette, as was previously reported for *Men1* KO mice (Scacheri et al., 2001; Bedogni et al., 2010). Alternatively,

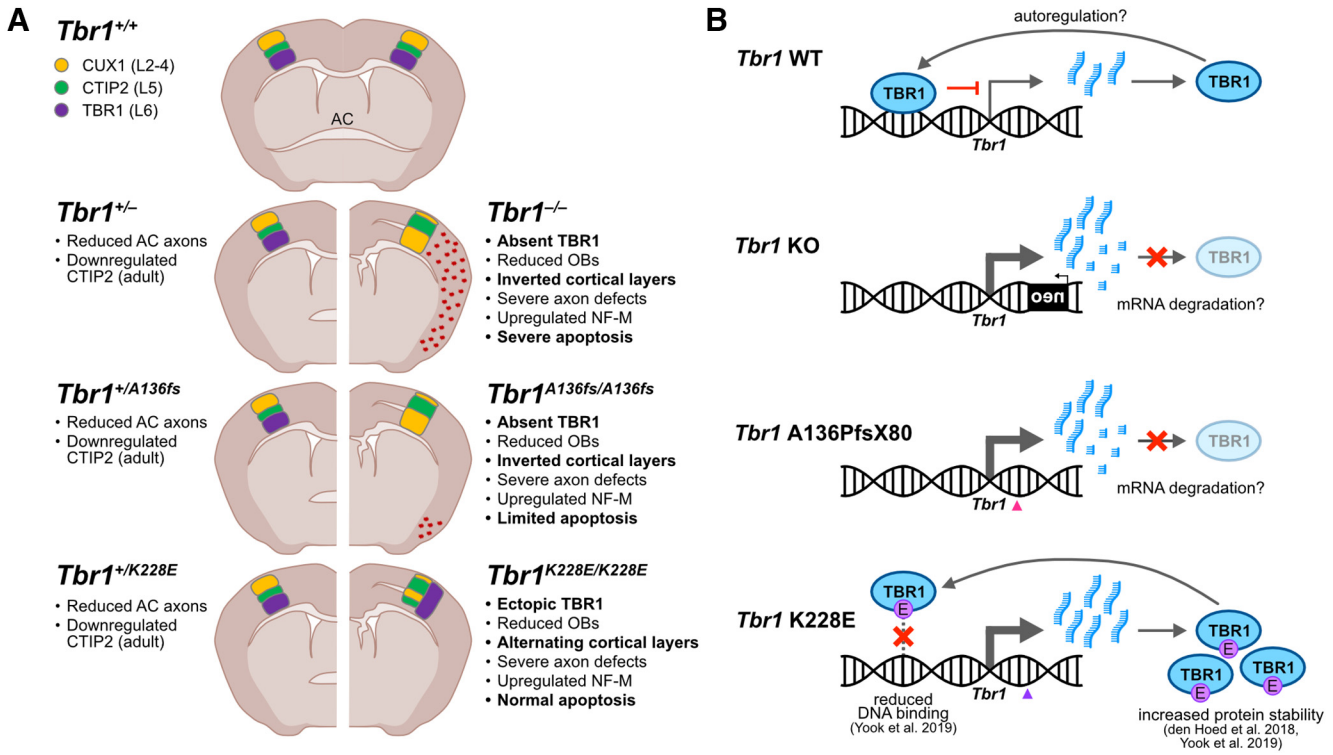

Figure 11. Summary of phenotypic findings and proposed molecular mechanisms in *Tbr1* mutant mice. ***A***, Summary of phenotypic findings in $Tbr1^{KO}$ line and patient mutant mouse lines $Tbr1^{A136fs}$ and $Tbr1^{K228E}$ compared with wild type. Phenotypes listed in bold text are discordant across the three mutant lines. ***B***, Proposed molecular effects of $Tbr1^{KO}$ and patient mutations on the regulation of TBR1 levels in postnatal cortex. TBR1 may negatively autoregulate its expression, leading to transcriptional upregulation in *Tbr1* mutant mice. Transcripts from the KO and A136fs alleles may be degraded, leading to the absence of TBR1 protein, while K228E transcripts persist and lead to high protein levels. OB, Olfactory bulb.

the neo cassette could disrupt regulatory elements within the *Tbr1* locus for nearby genes, in which case the *Tbr1* KO line could still serve to model intragenic *TBR1* deletions (Olson et al., 1996; Pham et al., 1996; Meier et al., 2010; Jin et al., 2021). Another example of a potential off-target effect is the altered interneuron distribution seen in previously generated K228E mutants, which retain an intronic loxP site (Yook et al., 2019). While this study found a shifted distribution of parvalbumin interneurons from superficial to deep layers in $Tbr1^{+/K228E}$ cortex, our CRISPR-generated $Tbr1^{+/K228E}$ mice showed no changes to the distribution of cortical interneurons (Fig. 7). However, this discrepancy could also arise from differences in cortical area examined, as the prior study analyzed medial prefrontal cortex while we analyzed somatosensory cortex.

Despite the potential limitations of previously generated *Tbr1* mouse models, they can recapitulate features of human *TBR1*-related conditions. Namely, in the study by Huang et al. (2014), $Tbr1^{+/-}$ mice showed reduction of the AC, a phenotype later observed in seven of seven individuals of a *TBR1* patient cohort examined by MRI (Nambot et al., 2020). Analysis of $Tbr1^{+/-}$ mice found an absence of the posterior limb of the AC using histologic stains, and axon labeling approaches showed severe reduction of the interamygdalar axons comprising this structure (Huang et al., 2014). A follow-up study also found a reduction of the anterior limb of the AC, which connects the two olfactory bulbs (Huang et al., 2019). When we immunostained for axon markers L1 and NF-M, $Tbr1^{+/A136fs}$ and $Tbr1^{+/K228E}$ mice lacked an apparent posterior limb, further reinforcing that this brain structure is highly sensitive to the mutation of one *Tbr1* copy (Fig. 8). We speculate that the posterior limb defect in *Tbr1* patient mutation mice could also be attributed to diminished interamygdalar axons, considering their similarity to $Tbr1^{+/-}$ mice analyzed alongside. Thus, *Tbr1* mutant mice with inserted DNA elements can be valid for modeling *TBR1* deficiency, but results should be interpreted with caution and, if possible, validated in multiple *Tbr1* mutant mouse lines.

In addition to our main findings, we observed that the p.E348_P353del (Δ6aa) mutation did not alter TBR1 levels (Figs. 2, 3) or cortical layer formation (Fig. 4). This result, combined with the low conservation of these residues among mouse T-box proteins (Fig. 1), suggests that substitutions or in-frame deletions within this region may not substantially impact TBR1 function. Accordingly, the reported human missense variants T350A, S351R, and P353A may be of low clinical impact as predicted by PolyPhen and SIFT analyses (Extended Data Fig. 1-1; Landrum et al., 2018; Karczewski et al., 2020). In contrast, the nonsense mutations S351X and Q352X show higher pathogenicity predictions, and the S351X protein was verified to be dysfunctional *in vitro* (Deriziotis et al., 2014). While TBR1-Δ6aa functionality is sufficient for corticogenesis, we cannot rule out subtler effects of this deletion on cortical development or neuronal function.

Potential *Tbr1* autoregulation in early postnatal cortex

Our analyses of *Tbr1* transcript and TBR1 protein levels provide insights into the regulation of this gene in early postnatal cortex (Fig. 11*B*). In P0 $Tbr1^{KO}$ and $Tbr1^{A136fs}$ mutants, transcript changes did not mirror protein changes: heterozygotes showed a 25–30% reduction in TBR1 protein but <8% reduction in *Tbr1* transcript, while homozygotes showed nearly 100% reduction in protein but only 25–60% reduction in transcript (Fig. 2). Based on these results, we speculate that TBR1 negatively autoregulates its expression in postnatal cortex, as transcription factors commonly perform autoregulatory functions to ensure proper abundance in cells (Crews and Pearson, 2009). Supporting this possibility,

TBR1-bound sites near the *Tbr1* gene (i.e., potential autoregulatory elements) have been previously identified using ChIP (chromatin immunoprecipitation)-sequencing (seq) assays in developing mouse cortex (Notwell et al., 2016; Fazel Darbandi et al., 2018). In $Tbr1^{KO}$ and $Tbr1^{A136fs}$ mutants, transcripts from the mutant allele may undergo nonsense-mediated decay or other mRNA degradation processes, as suggested by the low A136fs transcript levels in Figure 2*H*, leading to reduced TBR1 protein levels and reduced negative autoregulation. In $Tbr1^{K228E}$ mutants, the K228E mutation likely inhibits TBR1 binding to DNA, also leading to reduced negative autoregulation and increased *Tbr1* transcript/protein levels (Yook et al., 2019). The overabundance of TBR1 protein in these mice may also result from increased stability of the K228E protein (den Hoed et al., 2018; Yook et al., 2019).

Failure of negative autoregulation could also contribute to the unexpected ectopic TBR1 in nearly all cortical neurons of $Tbr1^{K228E/K228E}$ mice (Fig. 3). It has been postulated that the activation of TBR1 is an obligatory step in the differentiation of cortical radial glia into postmitotic neurons (Englund et al., 2005). Supporting this, single-cell RNA-seq of mouse corticogenesis found that cells born during the neurogenic period (embryonic days 12–15) highly express *Tbr1* on differentiation (http://genebrowser.unige.ch/telagirdon/; Telley et al., 2019). Newborn neurons then either maintain or repress *Tbr1* depending on their subtype specification: *Tbr1* is maintained in L6 corticothalamic neurons, while in other neuronal subtypes *Tbr1* is repressed by transcription factors including BCL11A (CTIP1) and FOXG1 (Toma et al., 2014; Cánovas et al., 2015; Liu et al., 2022). In non-corticothalamic neurons, negative autoregulation by TBR1 could perhaps then serve to inactivate its own expression through direct binding with its repressor BCL11A (den Hoed et al., 2018). Exploration of this hypothesis could lend important insights into TBR1-dependent regulatory networks and neuronal fate specification in the developing cortex.

Future directions

Future studies using patient-specific *Tbr1* mutant mice to model human conditions should focus on construct validity for underlying mechanisms, face validity for symptoms, and predictive validity for therapeutics. Molecular profiles and physiological properties of neurons should be compared across *Tbr1* mouse lines to identify shared etiologies. In addition, behavioral profiles should be characterized for comparison to *TBR1*-related conditions, particularly for anxiety, aggression, epilepsy, and other debilitating symptoms (Nambot et al., 2020). Testing therapeutics for such symptoms in *Tbr1* patient mutant mice could greatly benefit patients with *TBR1*-related or other neurodevelopmental conditions. Finally, beyond these translational directions, studying *Tbr1* patient mutant mice can inform our basic understanding of corticogenesis. We identified mutation-specific cortical layering defects, which hint at differential impacts on $TBR1^{+}$/$Reelin^{+}$ Cajal–Retzius cells during early cortical development (Fig. 4; Hevner et al., 2001). Furthermore, we identified ectopic intracortical axons in *Tbr1* mutants, but whether this defect arises cell autonomously from *Tbr1*-deficient projection neurons or is secondary to cortical disorganization in these mice remains unclear (Fig. 9). Future studies examining TBR1 functions in different cortical neuron subtypes can shed light on these fundamental neurodevelopmental processes.

References

Aida T, Chiyo K, Usami T, Ishikubo H, Imahashi R, Wada Y, Tanaka KF, Sakuma T, Yamamoto T, Tanaka K (2015) Cloning-free CRISPR/Cas system facilitates functional cassette knock-in in mice. Genome Biol 16:87.

American Psychiatric Association (2013) Neurodevelopmental disorders. In: Diagnostic and statistical manual of mental disorders: DSM-5, Ed 5. Washington, DC: American Psychiatric Association.

Bedogni F, Hodge RD, Elsen GE, Nelson BR, Daza RA, Beyer RP, Bammler TK, Rubenstein JL, Hevner RF (2010) Tbr1 regulates regional and laminar identity of postmitotic neurons in developing neocortex. Proc Natl Acad Sci U|S|A 107:13129–13134.

Bulfone A, Wang F, Hevner R, Anderson S, Cutforth T, Chen S, Meneses J, Pedersen R, Axel R, Rubenstein JL (1998) An olfactory sensory map develops in the absence of normal projection neurons or GABAergic interneurons. Neuron 21:1273–1282.

Cánovas J, Berndt FA, Sepúlveda H, Aguilar R, Veloso FA, Montecino M, Oliva C, Maass JC, Sierralta J, Kukuljan M (2015) The specification of cortical subcerebral projection neurons depends on the direct repression of TBR1 by CTIP1/BCL11a. J Neurosci 35:7552–7564.

Concordet J-P, Haeussler M (2018) CRISPOR: intuitive guide selection for CRISPR/Cas9 genome editing experiments and screens. Nucleic Acids Res 46:W242–W245.

Crews ST, Pearson JC (2009) Transcriptional autoregulation in development. Curr Biol 19:R241–R246.

den Hoed J, Sollis E, Venselaar H, Estruch SB, Deriziotis P, Fisher SE (2018) Functional characterization of TBR1 variants in neurodevelopmental disorder. Sci Rep 8:14279.

Deriziotis P, O'Roak BJ, Graham SA, Estruch SB, Dimitropoulou D, Bernier RA, Gerdts J, Shendure J, Eichler EE, Fisher SE (2014) De novo TBR1 mutations in sporadic autism disrupt protein functions. Nat Commun 5:4954.

Englund C, Fink A, Lau C, Pham D, Daza RA, Bulfone A, Kowalczyk T, Hevner RF (2005) Pax6, Tbr2, and Tbr1 are expressed sequentially by radial glia, intermediate progenitor cells, and postmitotic neurons in developing neocortex. J Neurosci 25:247–251.

Fazel Darbandi S, Robinson Schwartz SE, Qi Q, Catta-Preta R, Pai EL, Mandell JD, Everitt A, Rubin A, Krasnoff RA, Katzman S, Tastad D, Nord AS, Willsey AJ, Chen B, State MW, Sohal VS, Rubenstein JLR (2018) Neonatal Tbr1 dosage controls cortical layer 6 connectivity. Neuron 100:831–845.e7.

Fazel Darbandi S, Robinson Schwartz SE, Pai EL-L, Everitt A, Turner ML, Cheyette BNR, Willsey AJ, State MW, Sohal VS, Rubenstein JLR (2020) Enhancing WNT signaling restores cortical neuronal spine maturation and synaptogenesis in Tbr1 mutants. Cell Rep 31:107495.

Fazel Darbandi S, Nelson AD, Pai EL-l, Bender KJ, Rubenstein JLR (2022) LiCl treatment leads to long-term restoration of spine maturation and synaptogenesis in adult Tbr1 mutants. J Neurodev Disord 14:11.

Hamdan FF, Srour M, Capo-Chichi JM, Daoud H, Nassif C, Patry L, Massicotte C, Ambalavanan A, Spiegelman D, Diallo O, Henrion E, Dionne-Laporte A, Fougerat A, Pshezhetsky AV, Venkateswaran S, Rouleau GA, Michaud JL (2014) De novo mutations in moderate or severe intellectual disability. PLoS Genet 10:e1004772.

Han W, Kwan KY, Shim S, Lam MM, Shin Y, Xu X, Zhu Y, Li M, Sestan N (2011) TBR1 directly represses Fezf2 to control the laminar origin and development of the corticospinal tract. Proc Natl Acad Sci U|S|A 108:3041–3046.

Hevner RF, Shi L, Justice N, Hsueh Y, Sheng M, Smiga S, Bulfone A, Goffinet AM, Campagnoni AT, Rubenstein JL (2001) Tbr1 regulates differentiation of the preplate and layer 6. Neuron 29:353–366.

Hill JM, Lim MA, Stone MM (2008) Developmental milestones in the newborn mouse. In: Neuropeptide techniques (Gozes I, ed), pp 131–149. Totowa, NJ: Humana.

Huang TN, Chuang HC, Chou WH, Chen CY, Wang HF, Chou SJ, Hsueh YP (2014) Tbr1 haploinsufficiency impairs amygdalar axonal projections and results in cognitive abnormality. Nat Neurosci 17:240–247.

Huang TN, Yen TL, Qiu LR, Chuang HC, Lerch JP, Hsueh YP (2019) Haploinsufficiency of autism causative gene Tbr1 impairs olfactory discrimination and neuronal activation of the olfactory system in mice. Mol Autism 10:5.

Iakoucheva LM, Muotri AR, Sebat J (2019) Getting to the cores of autism. Cell 178:1287–1298.

Iossifov I, et al. (2014) The contribution of de novo coding mutations to autism spectrum disorder. Nature 515:216–221.

Jin C, Kang H, Yoo T, Ryu JR, Yoo Y-E, Ma R, Zhang Y, Kang HR, Kim Y, Seong H, Bang G, Park S, Kwon S-K, Sun W, Kim H, Kim JY, Kim E, Han K (2021) The neomycin resistance cassette in the targeted allele of

Shank3B knock-out mice has potential off-target effects to produce an unusual Shank3 isoform. Front Mol Neurosci 13:614435.
Karczewski KJ, et al. (2020) The mutational constraint spectrum quantified from variation in 141,456 humans. Nature 581:434–443.
Kwan KY, Šestan N, Anton ES (2012) Transcriptional co-regulation of neuronal migration and laminar identity in the neocortex. Development 139:1535–1546.
Landrum MJ, et al. (2018) ClinVar: improving access to variant interpretations and supporting evidence. Nucleic Acids Res 46:D1062–D1067.
Lee PH, et al. (2019) Genomic relationships, novel loci, and pleiotropic mechanisms across eight psychiatric disorders. Cell 179:1469–1482.e11.
Liu J, Yang M, Su M, Liu B, Zhou K, Sun C, Ba R, Yu B, Zhang B, Zhang Z, Fan W, Wang K, Zhong M, Han J, Zhao C (2022) FOXG1 sequentially orchestrates subtype specification of postmitotic cortical projection neurons. Sci Adv 8:eabh3568.
McDermott JH, Study DDD, Clayton-Smith J, Briggs TA (2018) The TBR1-related autistic-spectrum-disorder phenotype and its clinical spectrum. Eur J Med Genet 61:253–256.
McKenna WL, Betancourt J, Larkin KA, Abrams B, Guo C, Rubenstein JL, Chen B (2011) Tbr1 and Fezf2 regulate alternate corticofugal neuronal identities during neocortical development. J Neurosci 31:549–564.
McRae JF, et al. (2017) Prevalence and architecture of de novo mutations in developmental disorders. Nature 542:433–438.
Meier ID, Bernreuther C, Tilling T, Neidhardt J, Wong YW, Schulze C, Streichert T, Schachner M (2010) Short DNA sequences inserted for gene targeting can accidentally interfere with off-target gene expression. FASEB J 24:1714–1724.
Nambot S, et al. (2020) De novo TBR1 variants cause a neurocognitive phenotype with ID and autistic traits: report of 25 new individuals and review of the literature. Eur J Hum Genet 28:770–782.
Neale BM, et al. (2012) Patterns and rates of exonic de novo mutations in autism spectrum disorders. Nature 485:242–245.
Notwell JH, Heavner WE, Darbandi SF, Katzman S, McKenna WL, Ortiz-Londono CF, Tastad D, Eckler MJ, Rubenstein JL, McConnell SK, Chen B, Bejerano G (2016) TBR1 regulates autism risk genes in the developing neocortex. Genome Res 26:1013–1022.
Olson EN, Arnold HH, Rigby PWJ, Wold BJ (1996) Know your neighbors: three phenotypes in null mutants of the myogenic bHLH gene MRF4. Cell 85:1–4.
O'Roak BJ, et al. (2012a) Sporadic autism exomes reveal a highly interconnected protein network of de novo mutations. Nature 485:246–250.
O'Roak BJ, et al. (2012b) Multiplex targeted sequencing identifies recurrently mutated genes in autism spectrum disorders. Science 338:1619–1622.
O'Roak BJ, Stessman HA, Boyle EA, Witherspoon KT, Martin B, Lee C, Vives L, Baker C, Hiatt JB, Nickerson DA, Bernier R, Shendure J, Eichler EE (2014) Recurrent de novo mutations implicate novel genes underlying simplex autism risk. Nat Commun 5:5595.
Palumbo O, Fichera M, Palumbo P, Rizzo R, Mazzolla E, Cocuzza DM, Carella M, Mattina T (2014) TBR1 is the candidate gene for intellectual disability in patients with a 2q24.2 interstitial deletion. Am J Med Genet A 164A:828–833.
Pham CT, MacIvor DM, Hug BA, Heusel JW, Ley TJ (1996) Long-range disruption of gene expression by a selectable marker cassette. Proc Natl Acad Sci U|S|A 93:13090–13095.
Rueden CT, Schindelin J, Hiner MC, DeZonia BE, Walter AE, Arena ET, Eliceiri KW (2017) ImageJ2: ImageJ for the next generation of scientific image data. BMC Bioinformatics 18:529.
Scacheri PC, Crabtree JS, Novotny EA, Garrett-Beal L, Chen A, Edgemon KA, Marx SJ, Spiegel AM, Chandrasekharappa SC, Collins FS (2001) Bidirectional transcriptional activity of PGK-neomycin and unexpected embryonic lethality in heterozygote chimeric knockout mice. Genesis 30:259–263.
Telley L, Agirman G, Prados J, Amberg N, Fièvre S, Oberst P, Bartolini G, Vitali I, Cadilhac C, Hippenmeyer S, Nguyen L, Dayer A, Jabaudon D (2019) Temporal patterning of apical progenitors and their daughter neurons in the developing neocortex. Science 364:
Toma K, Kumamoto T, Hanashima C (2014) The timing of upper-layer neurogenesis is conferred by sequential derepression and negative feedback from deep-layer neurons. J Neurosci 34:13259–13276.
Vegas N, Cavallin M, Kleefstra T, de Boer L, Philbert M, Maillard C, Boddaert N, Munnich A, Hubert L, Bery A, Besmond C, Bahi-Buisson N (2018) Mutations in TBR1 gene leads to cortical malformations and intellectual disability. Eur J Med Genet 61:759–764.
Willsey AJ, et al. (2013) Coexpression networks implicate human midfetal deep cortical projection neurons in the pathogenesis of autism. Cell 155:997–1007.
Yook C, Kim K, Kim D, Kang H, Kim SG, Kim E, Kim SY (2019) A TBR1-K228E mutation induces Tbr1 upregulation, altered cortical distribution of interneurons, increased inhibitory synaptic transmission, and autistic-like behavioral deficits in mice. Front Mol Neurosci 12:241.
Yoon S, Munoz A, Yamrom B, Lee Y-h, Andrews P, Marks S, Wang Z, Reeves C, Winterkorn L, Krieger AM, Buja A, Pradhan K, Ronemus M, Baldwin KK, Levy D, Wigler M, Iossifov I (2021) Rates of contributory de novo mutation in high and low-risk autism families. Commun Biol 4:1026.